Author(s): Mahajan, Shreya; Lahtinen, Manu

Title: 3D Zinc–Organic Frameworks Based on Mixed Thiophene Dicarboxylate and 4-Amino-3,5-bis(4-pyridyl)-1,2,4-triazole Linkers : Syntheses, Structural Diversity, and Single-Crystal-to-Single-Crystal Transformations

Year: 2024

Version: Published version

CRYSTAL GROWTH & DESIGN

pubs.acs.org/crystal

Article

3D Zinc–Organic Frameworks Based on Mixed Thiophene Dicarboxylate and 4-Amino-3,5-bis(4-pyridyl)-1,2,4-triazole Linkers: Syntheses, Structural Diversity, and Single-Crystal-to-Single-Crystal Transformations

Shreya Mahajan and Manu Lahtinen*

Cite This: https://doi.org/10.1021/acs.cgd.3c01172

Read Online

ACCESS | Metrics & More | Article Recommendations | Supporting Information

ABSTRACT: In this study, for the first time two new interpenetrated 3D pillared-layer metal–organic frameworks (MOFs), namely, $\{[Zn(bpt)(tdc)]\cdot dmf\}_n$ (MOF-**1**-Zn) and $\{[Zn_2(bpt)(tdc)_2]\cdot 2(dmf)\}_n$ (MOF-**2**-Zn), as well as a homochiral 3D framework $\{[Zn(bpt)(tdc)(H_2O)]\cdot dmf\}_n$ (MOF-**3**-Zn), were prepared under different synthesis conditions (bpt = 4-amino-3,5-bis(4-pyridyl)-1,2,4-triazole, H_2tdc = 2,5-thiophenedicarboxylic acid, and dmf = *N*,*N*′-dimethylformamide). Synthesis products were thoroughly characterized by single-crystal and powder X-ray diffraction and thermoanalytical methods. Remarkably, in the case of MOF-**2**-Zn, dmf molecules in the voids can be exchanged for different solvents, e.g., chloroform, methanol, ethanol, isopropyl alcohol, acetonitrile, acetone, tetrahydrofuran, 1,4-dioxane, and cyclohexane in a single-crystal-to-single-crystal (SCSC) manner. With different solvent types, the bpt ligands adapted slightly different conformations by adjusting the orientation of the NH_2-triazole core unit and the tilting of the pyridyl groups. In comparison, most changes for planar tdc ligands were observed on the dihedral angles of the adjacent thiophene rings (e.g., 69.5 vs 78.5° for MOF-**2**-Zn and **2**-$CHCl_3$, respectively). Desolvation of the MOF illustrated systematic structural adaptability of $\{Zn_2\}$-"paddlewheel" in SCSC fashion, and the MOF's crystallinity and 3D networked structure were preserved even after vacuum and heat-assisted desolvation. Finally, preliminary CO_2 adsorption tests for MOFs were conducted utilizing a custom-built fixed-bed adsorption/desorption device, resulting in about 0.1 $mmol_{CO_2}/g_{sorbent}$ at 400–4000 ppmv CO_2 and about 1 $mmol_{CO_2}/g_{sorbent}$ at 15 vol % CO_2.

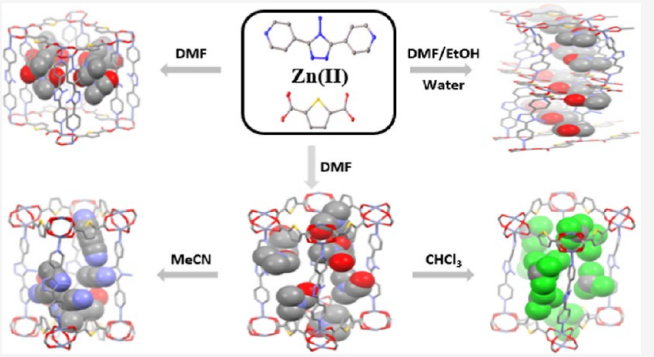

1. INTRODUCTION

Metal–organic frameworks (MOFs) are highly ordered crystalline structures possessing potential voids.[1] MOFs are derived from metal nodes linked by polytopic organic linkers and nowadays are at the forefront in the material science field and chemistry research.[2] Over the past few decades, MOFs have successfully established themselves as a highly competitive candidate for their practical utility in the plethora of chemistry-related fields varying from gas/liquid separations, storage applications, drug delivery, and chemical sensors to catalysis and beyond.[3−8] Among the wealth of MOFs, most structures have "rigid" networks and only limited examples have been reported to have structural flexibility as a characteristic feature of a MOF. In such cases, network structure can undergo a structural transition in response to a wide range of external chemical or physical stimuli (e.g., guest change and removal, heat, light, or mechanical pressure). Such structures form an appealing subclass of MOFs frequently recognized as flexible or breathing MOFs or simply soft porous crystals.[1,9−11]

In general, structural flexibility can be realized in different ways, including displacement of interpenetrated frameworks,[12] ligand motions,[13] and deformations at M–L bonds,[9] to name a few.[14] Thanks to single-crystal X-ray diffraction (SCXRD), these structural details can be directly determined and visualized. However, the shear force and stress generated by the solvent exchange can often significantly increase a crystal's mosaicity and fragmentation, resulting in unmeasurable single crystals. Therefore, single-crystal-to-single-crystal (SCSC) transformation is often challenging to observe structurally

Received: October 4, 2023
Revised: December 11, 2023
Accepted: December 12, 2023

and is a topical subject in the MOF community, as indicated by continually growing publishing output. Consequently, this phenomenon is a powerful tool for producing the most accurate property−structure correlations in atomic resolution. However, discovering new coordination frameworks that sustain sufficient crystallinity through the SCSC transformation is a continuous challenge.[11,15−18]

In this study, we present three new mixed-ligand MOFs prepared from identical starting components by mixing 4-amino-3,5-bis(4-pyridyl)-1,2,4-triazole (bpt) ligand, 2,5-thiophenedicarboxylic acid (H_2tdc), and $Zn(NO_3)_2$. Compositionally different MOFs were obtained concomitantly under identical solvothermal conditions, with a formula of $\{[Zn(bpt)(tdc)]\cdot dmf\}_n$ and $\{[Zn_2(bpt)(tdc)_2]\cdot 2(dmf)\}_n$, henceforth named MOF-**1**-Zn and MOF-**2**-Zn, respectively. The former MOF could also be isolated alone by a judicious selection of synthetic conditions. Along with attempts to optimize single-crystal growth and phase purity, a third structural modification with a formula of $\{[Zn(bpt)(tdc)(H_2O)]\cdot dmf\}_n$, named MOF-**3**-Zn, was also obtained.

The bpt ligand used in the syntheses was selected based on our previous studies,[19] wherein the ligand conformational changes were examined by crystallizing it from different mineral acids. Investigation resulted in 16 distinct crystal structures, demonstrating the ligand's ability to exhibit a versatile spectrum of molecular conformations ranging from planar to nearly perpendicularly tilted pyridyl end groups. To date, the bpt ligand has already been utilized in the MOF syntheses;[20−22] however, pairing it with the tdc ligand has not yet been reported. Second, considering aspects of a secondary building unit (SBU) with metal centers supported by carboxylates, tdc ligand may provide alternative binding modes, potentially endowing frameworks with unique coordination environments. Additionally, structural changes involving the "kneecap" rotational axis of the carboxylates may further contribute to a greater flexibility of the framework.[23]

With bpt, we envisaged that its versatile molecular conformations might enable structurally altered frameworks via a guest exchange, which could be monitored through SCSC transformations. Several solvents were employed to test whether they may replace dmf molecules and induce observable SCSC transformation. As a result, along with the crystal structures of three new pristine MOFs, their ten solvent exchange products and one desolvated crystal structure were obtained. Thermal stabilities of the crystalline products were also characterized by thermogravimetric analysis. Powder X-ray diffraction (PXRD) studies provided insights into the phase purity of bulk powders and in-depth structural insights into the framework's flexibility. In addition, the CO_2 adsorption capabilities of pillared-layer MOFs were also examined, utilizing a custom-built fixed-bed adsorption/desorption device under dry 400, 4000 ppm, and 15% CO_2 balanced with N_2.

2. METHODS

2.1. Material Syntheses and Characterization. The synthetic procedures for the 4-amino-3,5-bis(4-pyridyl)-1,2,4-triazole (bpt) ligand can be found in the Supporting Information. In general, the synthesis of bpt ligand followed the procedure reported in the literature.[19]

*2.1.1. Preparation of MOF-**1**-Zn.* A mixture of $Zn(NO_3)_2\cdot 6H_2O$ [120.19 mg, 0.404 mmol], 4-amino-3,5-bis(4-pyridyl)-1,2,4-triazole (bpt) [65.04 mg, 0.273 mmol], and thiophene-2,5-dicarboxylic acid (H_2tdc) [47.00 mg, 0.273 mmol] was added to dimethylformamide (dmf) [12 mL] in a Teflon-lined steel-made reaction vessel [22 mL] and heated at 120 °C for 72 h, followed by cooling to room temperature over a period of 24 h in an oven. The colorless plate-shaped crystals obtained were isolated by filtration, washed with dmf, and briefly air-dried (yield 117.70 mg, ∼78.84%, based on bpt). Anal. Calcd for $C_{21}H_{19}N_7O_5SZn$: C, 46.12; H, 3.50; N, 17.93. Found: C, 45.33; H, 3.33; N, 17.80%.

*2.1.2. Preparation of MOF-**2**-Zn.* A procedure similar to that of MOF-**1**-Zn was followed but with the exception of component ratio, as a 1:1:1 metal-to-ligands ratio was used instead of 1.48:1:1. The reaction produced simultaneously single crystals of MOF-**2**-Zn and MOF-**1**-Zn. The quantities used in the synthesis for $Zn(NO_3)_2\cdot 6H_2O$, bpt, H_2tdc, and dmf were [89.24 mg, 0.3 mmol], [71.48 mg, 0.3 mmol], [51.65 mg, 0.3 mmol], and [24 mL], respectively. Synthesis resulted in plate- and block-like single crystals, indicating the presence of both MOF-**1**-Zn and MOF-**2**-Zn, respectively. The colorless crystals obtained were filtered, washed with dmf, and briefly dried in air (yield 120.30 mg, % yield, and EA not calculated because of a mixture).

*2.1.3. Preparation of MOF-**3**-Zn.* $Zn(NO_3)_2\cdot 6H_2O$ [44.92 mg, 0.151 mmol], bpt [23.83 mg, 0.1 mmol], and H_2tdc [17.22 mg, 0.1 mmol] were dissolved separately in deionized water [5 mL], hot ethanol EtOH [30 mL], and dmf [5 mL], respectively. A clear solution of the zinc salt and bpt was mixed, and subsequently, the H_2tdc solution was added dropwise to this solution with vigorous stirring at 80 °C. After 1 h, the cooled solution was filtered to remove the remaining residue. Finally, colorless rod-shaped crystals were afforded by slow solvent evaporation at room temperature from the resulting solution within a week. The crystals obtained were decanted from the mother liquor and stirred in fresh dmf for a few hours to ensure the removal of unreacted materials and unwanted species and then dried in air (yield 17.30 mg, ∼30.63% based on bpt). Anal. Calcd for $C_{21}H_{21}N_7O_6SZn$: C, 44.65; H, 3.75; N, 17.36. Found: C, 44.37; H, 3.53; N, 17.07%.

2.2. Single-Crystal X-ray Diffraction. Single crystals suitable for the SCXRD analyses were typically picked directly from the crystallization solvent. For testing solvent exchange, fresh crystals of pristine MOF type were submerged into the desired solvent for 2−7 days, and the solvent was changed at 12- or 24 h intervals three times (more details in the Supporting Information).

Crystal data for MOF-**1**-Zn, MOF-**2**-Zn, MOF-**3**-Zn, and for other samples were collected sample dependently by Rigaku XtaLAB Synergy-R high flux rotating anode X-ray diffractometer equipped with HyPix-Arc 100° curved photon counting detector, and PhotonJet-R source with MicroMax-007 rotating anode (Cu K_α, λ = 1.54184 Å); Rigaku SuperNova single-source diffractometer (Eos CCD detector) using mirror-monochromatized Mo K_α radiation (λ = 0.71073 Å); or Rigaku SuperNova dual-source (Cu and Mo microsources) X-ray diffractometer equipped with Atlas CCD detector (for few samples, HyPix-Arc 100°) and multilayer optics producing monochromatized Cu K_α radiation (λ = 1.54184 Å). Data collection, reduction, and analytical face-index-based absorption correction methods were performed using the CrysAlisPRO[24] program. All structures were solved by the ShelXT[25] (intrinsic phasing) program implemented in the Olex^2(v.1.5)[26] and refined on F^2 by full-matrix least-squares techniques with the ShelXL[27] program. All non-hydrogen atoms were refined anisotropically. Hydrogen atoms were calculated to their ideal positions using isotropic temperature factors 1.2 or 1.5 times their parent atom and were refined as riding atoms. Occupancies of disordered moieties were first determined using free variables in the refinement but, at the final stages, were typically fixed to help converge the refinement, particularly in the case of solvent molecules with low occupancies. Electron densities of severely disordered solvents were removed on the final refinement of the structure through the OLEX^2 solvent mask (SM) tool after their chemical composition was confirmed first (when applicable). The removed electron density was not considered when determining the chemical formula. The contact surface calculations to determine void spaces (radius: 1.2 Å) and figures were generated by the Mercury program.[28] Further details about all of the SCXRD structures can be found in the provided crystallographic information

https://doi.org/10.1021/acs.cgd.3c01172
Cryst. Growth Des. XXXX, XXX, XXX−XXX

Scheme 1. Representation of tdc^{2-} Carboxylate Group Binding Modes, Dihedral Angles between the Two-Pyridine Rings and the Central Triazole Ring of bpt, Coordination Geometry around Zn^{II} Ion in MOF-1-Zn, MOF-2-Zn, and MOF-3-Zn, Respectively; Only Relevant Atoms Are Shown

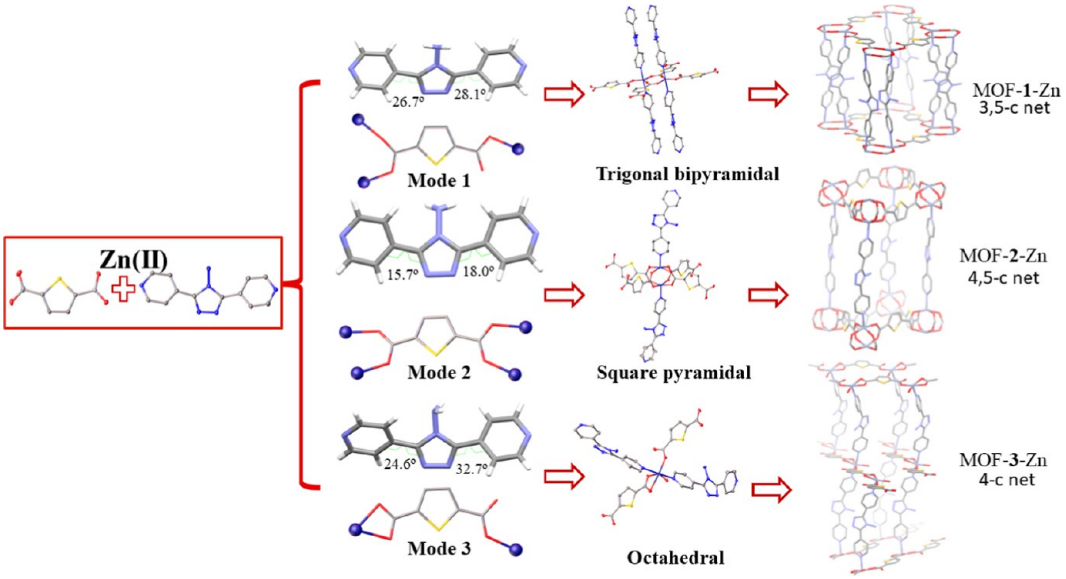

files deposited at the Cambridge Crystallographic Data Centre (CCDC) under deposition numbers CCDC 2279907 [MOF-**1**-Zn], 2279908 [MOF-**2**-Zn], 2279909 [MOF-**3**-Zn], 2279898 [**2**-CH_3Cl], 2279904 [**2**-MeOH], 2279901 [**2**-EtOH], 2279902 [**2**-*i*-PrOH], 2279903 [**2**-MeCN], 2279897 [**2**-acetone], 2279905 [**2**-THF], 2279900 [**2**-dioxane], 2279899 [**2**-cyclohexane], 2279906 [guest-freed, **2**-gf], and 2279896 [**1**-MeOH].

2.3. Powder X-ray Diffraction. PXRD data were measured using a Panalytical X'Pert PRO MPD diffractometer with Cu K_α radiation (λ = 1.54184 Å; Ni β-filter; 45 kV, 40 mA). Each powder sample was placed on a silicon-made "zero-background signal generating" plate using petrolatum jelly as an adhesive. Diffraction intensities were recorded by an X'Celerator detector at room temperature with 2θ-range of 3−60°, a step size of 0.017°, and a counting time of 70 s per step. Data processing, search-match phase analyses, and Pawley whole-pattern fits were carried out by the program X'pert HighScore Plus (v. 4.9). Search-match phase identification analyses were made against the ICDD-PDF4+ database (version 2022) implemented in the HighScore.[29,30] In the Pawley fits, the unit cell parameters of the PXRD patterns were refined using the corresponding single crystal structure parameters as the basis of least-squares refinement. Variables for the fits were as follows: zero-offset, polynomial background, sample height displacement, unit cell parameters, and peak profile parameters, including peak width, shape, and asymmetry.

2.4. Thermal Analysis. The thermal properties of the compounds were examined using a PerkinElmer STA 6000 simultaneous thermogravimetric-calorimetric TG/DSC analyzer. Each sample was measured in an open platinum pan and heated under an N_2 atmosphere (flow rate of 40 mL/min) with a heating rate of 10 °C/min on a temperature range of 22−600 °C. For each run under N_2, 10 min isotherm at 22 °C was introduced to ensure proper purging of the furnace interior from the ambient air atmosphere before the start of the heating step. Temperature calibration of the analyzer was made using melting points of the indium (156.6 °C), zinc (419.5 °C), and aluminum (660.3 °C) standards. The weight balance was calibrated at room temperature using a standard weight of 50.00 mg. The sample weights used in the measurements were about 1−8 mg.

2.5. CO_2 Adsorption Tests. CO_2 adsorption tests were conducted at VTT Technical Research Centre of Finland using a custom-built fixed-bed adsorption/desorption device used earlier for lab-scale direct air capture experiments with an amine-functionalized resin.[31,32] Approximately, 100 mg of the MOF sample was packed into the adsorption column with quartz wool below and above the adsorbent bed. The sample was first regenerated using nitrogen purge at 100 °C, then cooled down to the adsorption temperature of 12 °C. Adsorption was then initiated using dry 400, 4000 ppm, or 15% CO_2 balanced with N_2. Desorption was carried out at 100 °C using N_2. The total flow rate was 200 mL/min, corresponding to a superficial velocity of 0.052 m/s inside the column. The CO_2 capacities were calculated by numerical integration of the flow rate and CO_2 concentration profiles and using the ideal gas law.

The effect of the dead volume of the adsorption rig and the CO_2 analyzer lag was considered by measuring CO_2 capacities in the same conditions without a sample and subtracting these capacities from the ones measured with the sample. The adsorption results in the 15% CO_2 tests were measured using a %-scale CO_2 analyzer, while the desorption results were measured using the ppm-scale sensor. Although the ppm-scale sensor only measured up to 5000 ppm, its higher accuracy in the ppm region allowed for better comparison between the two samples. However, for this reason, it should be noted that the reported desorption results may be lower than the actual total desorption capacity, and care should be taken in comparison to literature values. More details of the experimental device and the calculation methods can be found in ref 33 while an in-depth discussion of the experimental uncertainty of the device is available elsewhere.[32] The methanol-exchanged MOF-**1**-Zn sample was activated at 120 °C overnight under vacuo, and the mixture was heated at 180 °C overnight under vacuo before the CO_2 adsorption tests.

3. RESULTS AND DISCUSSION

3.1. Syntheses and Structure. All three compounds, MOF-**1**-Zn, MOF-**2**-Zn, and MOF-**3**-Zn, were synthesized under somewhat different synthetic conditions, resulting in structures with distinct void volumes, featuring different coordination geometries, binding modes, and alignments of organic ligands, as well as dissimilar topologies (Scheme 1). MOF-**1**-Zn and MOF-**2**-Zn, as well as their mixtures, resulted from solvothermal reactions (at 120 °C) using different metal-to-ligand ratios and solvent volumes (more details in the Supporting Information). MOF-**3**-Zn was obtained by slow evaporation from an EtOH/water/dmf solvent mixture. All three crystal structures were solved by SCXRD. The reaction

https://doi.org/10.1021/acs.cgd.3c01172
Cryst. Growth Des. XXXX, XXX, XXX−XXX

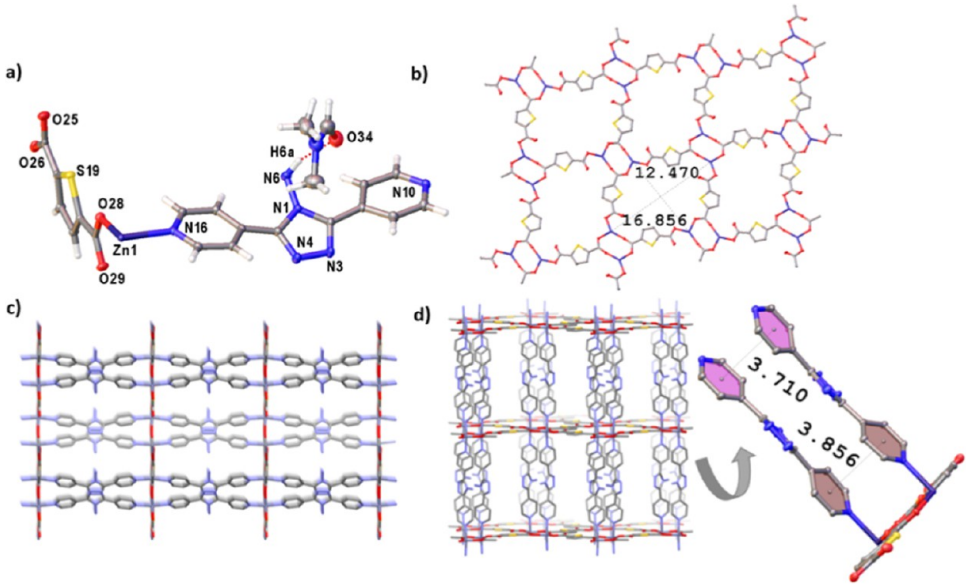

Figure 1. Depiction of the crystal structure of MOF-**1**-Zn. (a) Coordination environment around Zn^{II}, (b) partial view of 2D networked layer, and (c,d) views of the single-net 3D pillared-layer framework along the *a*- and *c*-axes, respectively, with a view of $\pi-\pi$ interactions between bpt ligands. All hydrogen atoms are omitted for clarity; only relevant atoms are shown; interatomic distances are given in Å (applies to all figures).

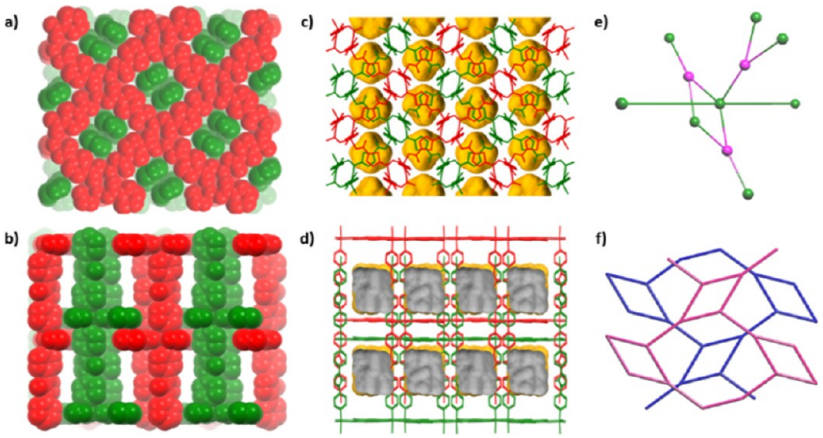

Figure 2. Depiction of the crystal structure of MOF-**1**-Zn. (a,b) Space-filling representation of 2-fold interpenetration (red and green) along the *b*- and *c*-axes, respectively, (c,d) potential void space visualized by yellow/gray (outer/inner) colors, and (e,f) simplified view of a (3,5)-connected network.

of bpt, H_2tdc, and $Zn(NO_3)_2{\cdot}6H_2O$ in a molar ratio 1:1:1.48 at 120 °C for 72 h resulted in MOF-**1**-Zn obtained as plate-shaped crystals. It is built on trigonal bipyramidal coordination geometry where tdc^{2-} adopts coordination mode 1 (Scheme 1). Under the same conditions but with a changed concentration and a molar ratio of 1:1:1, it resulted in a mixture of MOF-**1**-Zn and MOF-**2**-Zn, entailing the same metal and organic building blocks. MOF-**2**-Zn was obtained as block-shaped crystals built on paddlewheel units, where each tdc^{2-} adopts alternative bridging mode 2 (Scheme 1). The underlying reason for the dissimilar geometries of SBU could be that both trigonal bipyramidal and square pyramidal coordination geometries have nearly the same energies. Thus, the switching from trigonal bipyramidal to square pyramidal or vice versa is reasonably straightforward.[34] From the available literature, we know that paddlewheel core is common in flexible MOFs with zinc- and copper-based systems, and the Zn-based paddlewheel MOFs have overall lower stability and higher flexibility in comparison to copper-based systems attributed to respective electronic structures [d^{10} Zn(II) and d^9 Cu(II)].[35] Contrarily, Zn^{II} in MOF-**3**-Zn adopted octahedral geometry instead of trigonal bipyramidal or square pyramidal, as in this case, water molecules (solvent) interfere by directly coordinating to the Zn center, in contrast to solvothermal conditions wherein dmf molecules do not show any interaction with a metal center. Significant differences observed between the frameworks are further examined in detail in Sections 3.1.1−3.1.3. Crystallographic data and the selected structure refinement parameters are summarized in (Table S1).

3.1.1. Crystal Structure of MOF-1-Zn. Based on the X-ray crystallographic structure determination, MOF-**1**-Zn crystallizes in the orthorhombic space group *Pcca* (Figure 1a), having a single Zn^{II}, bpt ligand, fully deprotonated tdc^{2-} ligand, and a single dmf molecule in an asymmetric unit (AU). As visualized in Scheme 1, the Zn^{II} center site, exhibiting a distorted trigonal bipyramidal coordination geometry, is defined by three carboxylate oxygen atoms from three tdc^{2-} ligands located in

https://doi.org/10.1021/acs.cgd.3c01172
Cryst. Growth Des. XXXX, XXX, XXX−XXX

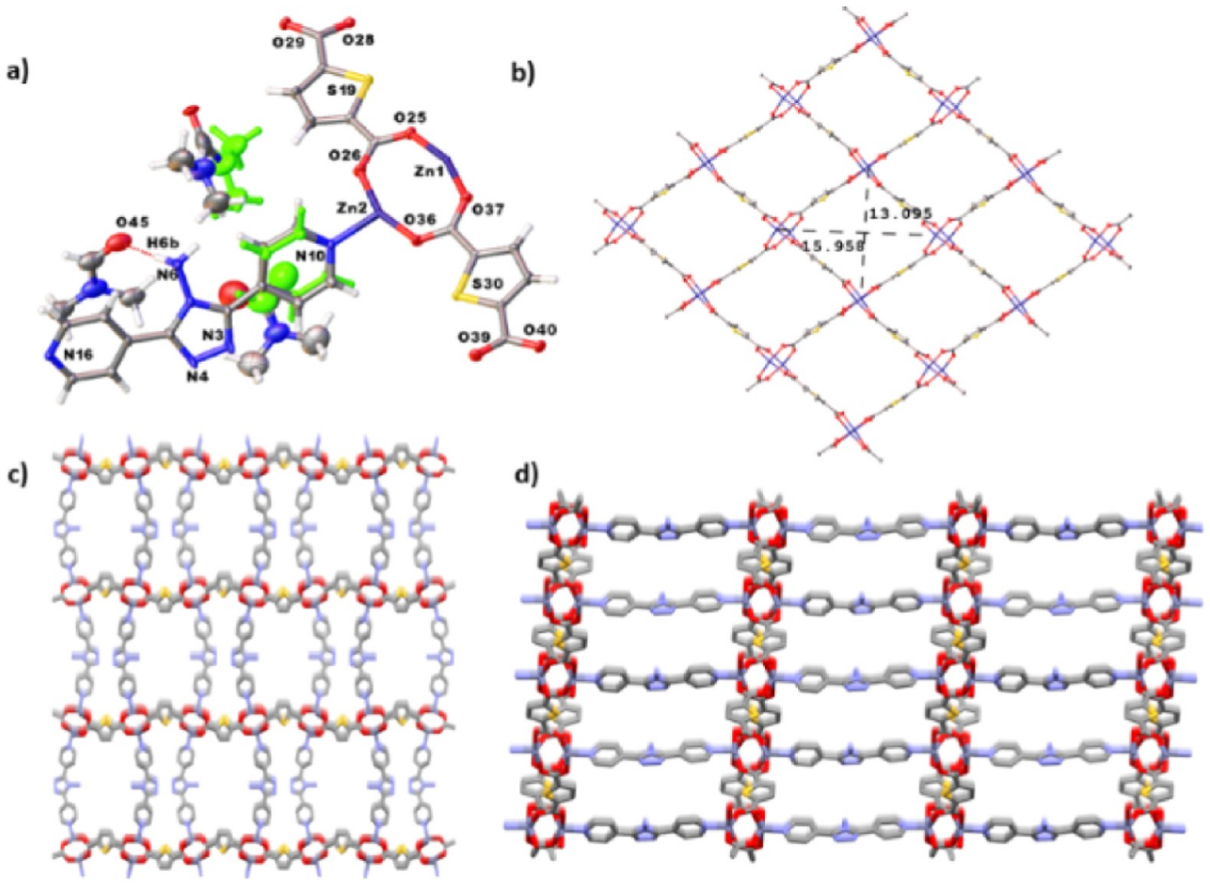

Figure 3. Depiction of the crystal structure of MOF-**2**-Zn. (a) Coordination environment around the Zn^{II}, (b) view of the 2D networked layer, and (c,d) views of the single-net 3D pillared-layer framework along the *a*- and *b*-axes, respectively.

the equatorial plane. Two pyridyl nitrogen atoms (N10 and N16) from two bpt ligands occupy the axial positions, respectively. Both pyridyl rings of the bpt ligand feature almost equal and significant twisting in parallel directions with respect to the central triazole ring, as manifested by dihedral angles 26.79(11) and 28.17(11)°, respectively.

Herein, each tdc^{2-} adopts binding mode 1 (Scheme 1), bound to three different Zn^{II}, where one carboxylate group adopts monodentate and the other carboxylate functions as bridging mode, respectively. Thus, the dimeric unit built by carboxylate groups separates Zn···Zn by 4.1655(6) Å and propagates along the *ac*-plane to form a planar 2D layer with square grid dimensions of about 12.4699(7) × 16.8556 (5) $Å^2$ (based on Zn···Zn separation) along the *b*-axis (Figure 1b). Furthermore, the neutral ditopic bpt ligands act as pillars where each bpt coordinates with two Zn^{II} by its two pyridyl end groups to interconnect the resulting 2D layers, affording a 3D pillared-layer MOF (Figure 1c,d). Interestingly, two similar 3D nets interpenetrate each other in such a way that a 2-fold interpenetrating network holds 23.4% solvent-accessible void corresponding to ∼1026 $Å^3$ volume, as determined by contact surface calculations (Figure 2).

The structure of MOF-**1**-Zn is also stabilized both by $\pi-\pi$ interactions between the adjacent pyridyl groups of bpt with a centroid−centroid $d(\pi-\pi)$ distance being 3.710(2)−3.856(2) Å, and via framework−solvent interactions involving between pendant $-NH_2$ group of bpt pillar and the oxygen atom of the solvent molecule (dmf). Topological examination of the MOF-**1**-Zn structure made with the ToposPro program reveals the structure to be an unusual (3,5)-connected net (Figure 2e,f).[36]

*3.1.2. Crystal Structure of MOF-**2**-Zn.* MOF-**2**-Zn crystallizes in a monoclinic *I*2/*a* space group and has two Zn^{II} atoms, one bpt ligand, two fully deprotonated tdc^{2-} ligands, and two disordered dmf guest molecules in an AU. One pyridyl group is disordered over two positions with approximate occupancies of 0.6:0.4 on its carbon atoms (Figure 3a). Each Zn^{II} furnishes a distorted square-pyramidal $[ZnO_4N]$ geometry coordinated equatorially to four oxygen atoms from four different tdc^{2-} ligands and apically to one nitrogen atom of the bpt ligand. Unlike in MOF-**1**-Zn, each tdc^{2-} in MOF-**2**-Zn adopts binding mode 2 (Scheme 1), wherein Zn^{II} is in a bridging mode and as a result $[Zn_2(tdc)_2]$ lattice forms rhombic grids with diagonal distances about ca. 13.0950(3) × 15.9577(4) $Å^2$ along the crystallographic *c*-axis (Figure 3b). In terms of nodal geometry (SBU), Zn-node is a typical $\{Zn_2\}$-"paddlewheel", which is bridged by bpt pillars along the axial position of the paddlewheel, and in overall furnishing 3D pillared-layer MOF-**2**-Zn (Figure 3c,d). Compared to MOF-**1**-Zn, some characteristic differences in the molecular conformation of the pillar can be noted as the MOF-**2**-Zn does not contain any $\pi-\pi$ stacking interactions of bpt pillars. In addition, there are noticeable differences in dihedral angles between the pyridyl groups and the central triazole ring, indicating modest tilting of the pyridyl groups with the central triazole ring [18.0(3) and 15.73(18)°]. The 2D layers in MOF-**2**-Zn are kind of corrugated, whereas in MOF-**1**-Zn, they are planar. However, MOF-**2**-Zn is also an interpenetrated 3D framework (Figure

https://doi.org/10.1021/acs.cgd.3c01172
Cryst. Growth Des. XXXX, XXX, XXX−XXX

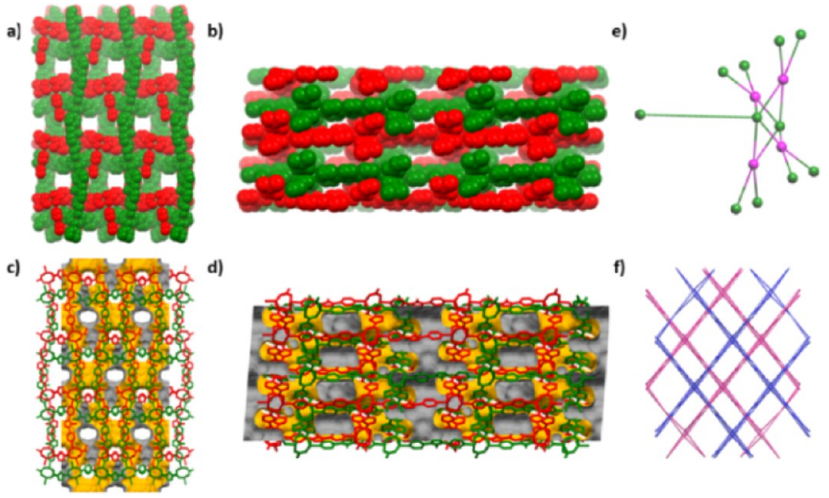

Figure 4. Partial views of MOF-**2**-Zn crystal structure. (a,b) Space-filling representation of 2-fold interpenetration along the *a*- and *b*-axes, respectively, (c,d) potential void space visualized by yellow/gray (outer/inner) colors, and (e,f) simplified view of a (4,5)-connected network.

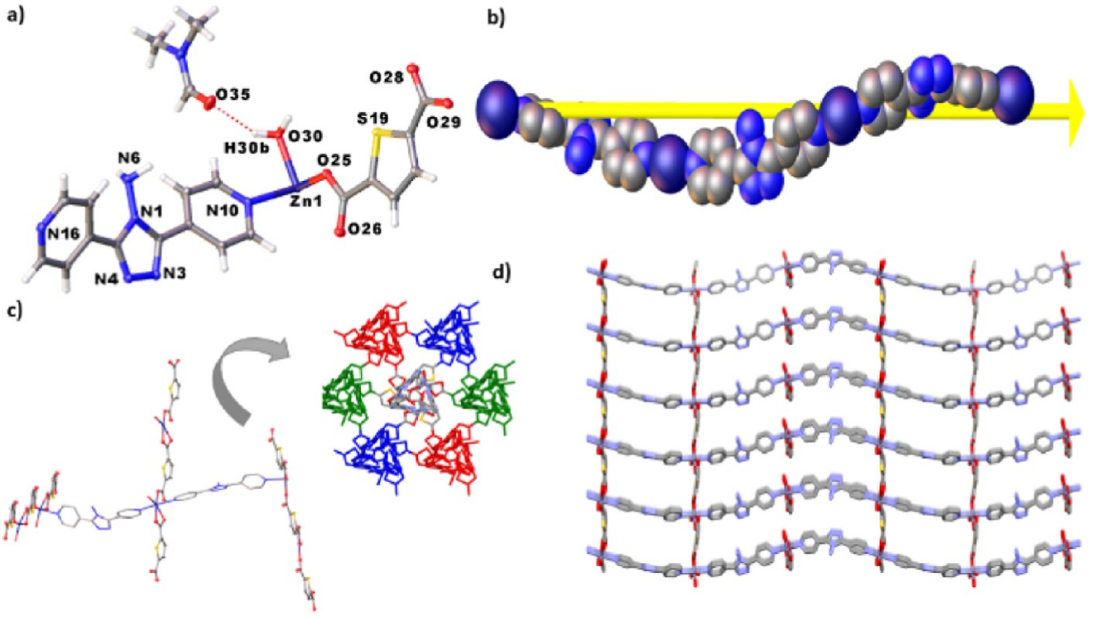

Figure 5. Depiction of the crystal structure of MOF-**3**-Zn. (a) Coordination environment around Zn^{II}, (b) space-filling view of the 3_1-helix along the *b*-axis, (c) view of three different orientations of tdc^{2-} linkers (A: blue, B: red, and C: green), and (d) single-net of the 3D framework along the *b*-axis.

4a,b) having an adequate free volume of 35.3% (corresponding to 2544 $Å^3$ when solvents are removed), as shown in Figure 4c,d. Topologically, MOF-**2**-Zn can be represented as (4,5)-connected net (Figure 4e,f).

*3.1.3. Crystal Structure of MOF-**3**-Zn.* MOF-**3**-Zn features a homochiral 3D framework with high hexagonal symmetry (space group $P6_1$) formed despite achiral bpt and tdc^{2-} ligands. As illustrated in Figure 5a, AU consists of a single Zn^{II}, bpt, fully deprotonated tdc^{2-} ligand, single water coordinated to the Zn, and one dmf molecule hydrogen-bonded to the coordinated water molecule. In MOF-**3**-Zn, Zn^{II} adopts a distorted octahedral geometry containing three carboxylate oxygen atoms from two tdc^{2-} ligands, one in monodentate and the other in chelating binding mode (mode 3, Scheme 1), as well as one oxygen atom of a water molecule, and two pyridyl nitrogen atoms from two adjacent bpt ligands.

Notably, both the pyridyl rings of the bpt ligand are significantly tilted in the opposite direction relative to each other [56.61(10)°]. Dihedral angles of the pyridyls to the central triazole ring are 24.69(11) and 32.73(11)°, respectively. Overall, infinite single-stranded one-handed wavy 3_1-helices are formed via Zn-bpt bridging that progress along the *c*-axis. All helical chains are arranged in parallel and are further interconnected, forming the 3D honeycomb framework along the *c*-axis, as shown in Figure 5. Described interconnections are formed via tdc^{2-} ligands, which bind to Zn^{II} by a single carboxylate in bidentate and the other one in monodentate fashion to form 1-D linear chains that are rotated by 120° along the crystallographic *c*-axis. These chains, while passing from one to the next successive layer, possess three different orientations (Figure 5c).

Noteworthily, MOF-**3**-Zn features a 2-fold interpenetrating network (Figure 6a,b) wherein the subnets interact via

https://doi.org/10.1021/acs.cgd.3c01172
Cryst. Growth Des. XXXX, XXX, XXX−XXX

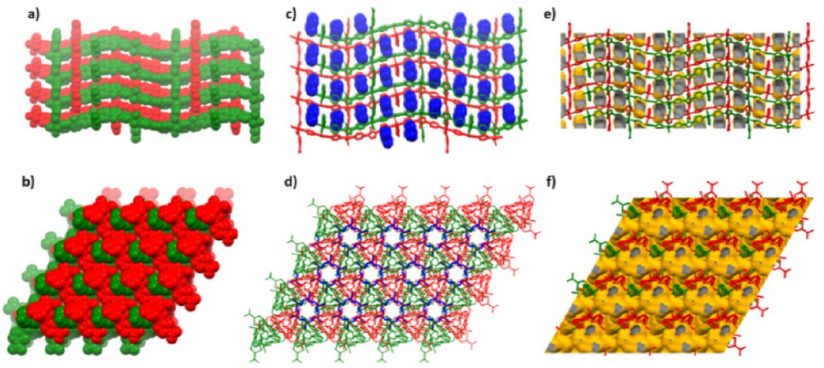

Figure 6. Depiction of the crystal structure of MOF-**3**-Zn. (a,b) Space-filling representation of 2-fold interpenetration along the *b*- and *c*-axes, respectively, (c,d) dmf (in blue) filled channels viewed along the *b*- and *c*-axes, respectively, and (e,f) potential void space along the *b*- and *c*-axes respectively, visualized by yellow/gray (outer/inner) colors.

multiple hydrogen-bond interactions involving coordinated water molecule and the nitrogen atom of the triazole ring [d(O···N) = 2.69 Å]. Moreover, the $-NH_2$ group of bpt ligand is H-bonded to both the coordinated as well as uncoordinated carboxyl groups on the tdc^{2-} linkers with d(N−O) distances of ∼2.82−2.89 Å (Figure S1a). When viewed along the *b*-axis, the channels are filled with dmf molecules in a row formation, arranged as hexagonal helical chains along the *c*-axis (Figure 6c,d). The guest-freed MOF-**3**-Zn incorporates a potential free volume of about 22.9%, equivalent to ∼812 $Å^3$ (Figure 6e,f). Topologically, MOF-**3**-Zn exhibits a uninodal 4-connected net (Figure S1b), which differs from the nets in MOF-**1**-Zn and MOF-**2**-Zn, respectively.

3.2. Single-Crystal-to-Single-Crystal Guest Exchange. The presence of elastic paddlewheel units in the pillared-layer MOFs typically endows the framework with inherent flexibility.[1,37,38] With this in mind, the guest-exchange properties of MOF-**2**-Zn (henceforth **2**) were further examined to observe whether solvents can be removed and introduced to the voids in the single-crystal-to-single-crystal (SCSC) manner. The first solvent selected for the tests was chloroform, widely used in MOF-activation procedures (Figure 7). In the

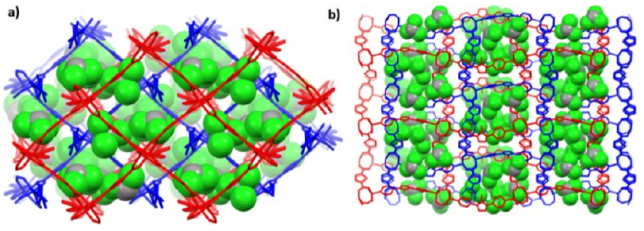

Figure 7. Crystal structure illustration of **2**-$CHCl_3$. The 2-fold interpenetration (red and blue nets) of a 3D pillared framework displaying accommodated chloroform molecules (space-fill representation) along the (a) *a*-axis and (b) *c*-axis.

experiment, single crystals of **2** were submersed in chloroform for 48 h under ambient conditions (Figure 8). Crystals obtained from the solvent exchange showed some cracking and some degree of fragmentation for larger crystals. However, there was no evident change in color (still transparent), and the fact that even the crystal fragments retained their crystalline features; some crystals were subjected to SCXRD analysis. As a result, the solvent exchanged **2**-$CHCl_3$ crystallizes in the $P2_1/c$ space group ($I2/a$ for **2** with dmf in the pores), and the asymmetric unit comprises four Zn^{II}, two bpt ligands of which one triazole and pyridyl ring of a single bpt are disordered over two locations with occupancies of 0.85:0.15. The AU also contains four fully deprotonated tdc^{2-} linkers and 3.85 $CHCl_3$ molecules, of which all except one $CHCl_3$ are disordered. A single $CHCl_3$ is disordered over two locations (0.9:0.1), whereas one $CHCl_3$ shows partial Cl disorder over two locations (0.6:0.4), and a single $CHCl_3$ with 0.85 occupancies and is located as disorder pair for the disordered pyridyl group of bpt. Compared to structure **2**, the volumetric (V) change of the new unit cell is −0.49%, the β-angle increases by +1.08% while more markedly *a*-, *b*-, and *c*-axes change by +6.08, −5.20 and −0.89%, respectively as shown by the unit cell parameters of **2** and **2**-$CHCl_3$, respectively: a = 13.095/13.890 Å, b = 15.957/15.127 Å, c = 34.566/34.259 Å, β = 94.306/95.321, and V = 7202/7167 $Å^3$.

The exchange of $CHCl_3$ molecules to the structure of **2** induces the most pronounced changes in the pillar region (Figure 9). Interestingly, the changes in the shape of the channels (Figure S2) are provoked by the changes in molecular conformations of the pillars (bpt), which are accompanied by subtle alterations in the metal-carboxylate bonding scheme. Evidently, two Zn^{II} nodes and pillared ligands deviate slightly from linearity, as indicated by the N−Zn···Zn−N torsion angles, which were changed from 163.5(15) to 157.2(16)/179.2(19)° for **2** and **2**-$CHCl_3$, respectively. Concurrently, across the bpt direction (Zn···Zn-(bpt)-Zn···Zn), the Zn_2···Zn_2 angles have clearly changed from 32.45(8) to 22.49(10)/36.60(9)°, respectively. The modest variation in the angle between the Zn−N coordination bond and the pyridine plane (angle of ligation) and the angle between the $C_{triazole}$−$C_{pyridine}$ covalent bond and pyridine plane are further responsible for the observed distortion on the Zn_2···Zn_2 angles. The conformational flexibility of the pillar can also be verified by broadly varied tilting between the pyridyl and triazole rings, as shown by the range of dihedral angles 18.0(3)−15.73(18) and 22.1(3)−28.3(3)/30.3(3)−31.2(2)° for **2** and **2**-$CHCl_3$, respectively. In the case of structure **2**, both pyridyl rings are almost perfectly aligned on the same plane in relation to each other [5.8(2)°], whereas, in the **2**-$CHCl_3$, pyridyls are strongly tilted in opposite directions to each other [dihedral angle ∼60.6(3)°]. Besides tilting the pyridyl units, the bpt pillar can readjust the NH_2-triazole ring in response to the guest solvent (Figure 8). The angle "Ø", defined as the angle between two adjacent planes of triazole rings, describes the orientation of the triazole core. Particularly, the change in the orientation of the triazole core from 45.9(3) to 37.7(5)/40.0(4)° in part

https://doi.org/10.1021/acs.cgd.3c01172
Cryst. Growth Des. XXXX, XXX, XXX−XXX

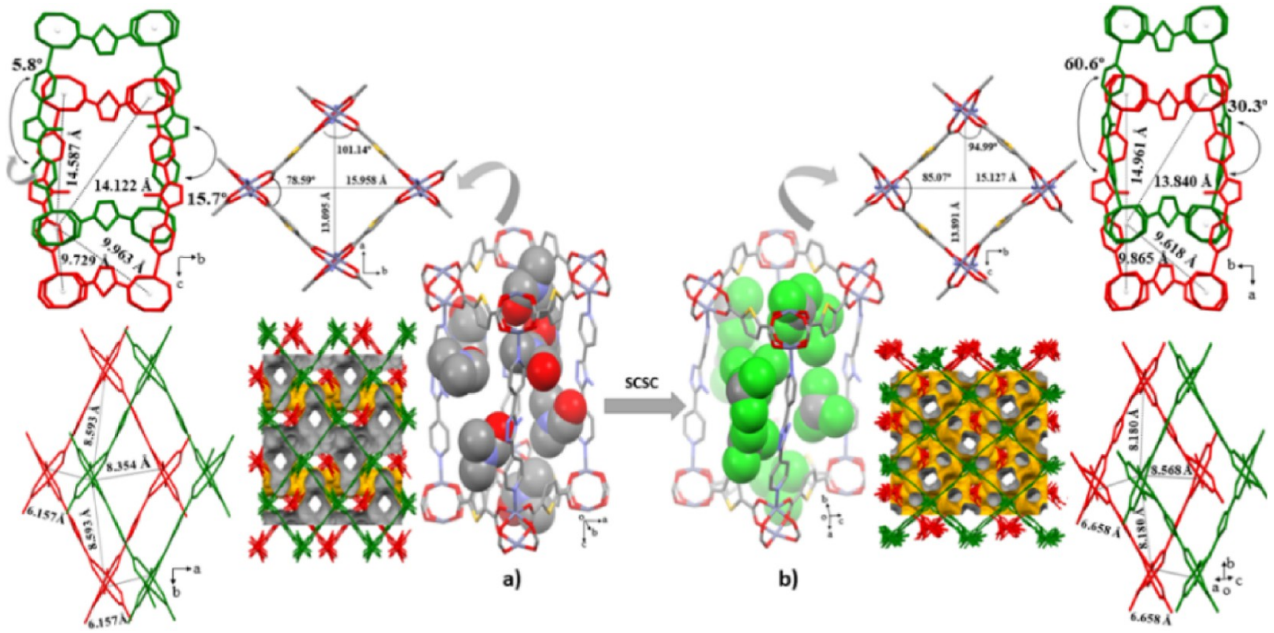

Figure 8. Guest-responsive SCSC structural transformation determined by SCXRD. Views in (a) **2** (with dmf) and (b) **2**-$CHCl_3$ "image sides" demonstrate structural transformation along the pillar (bpt)-axis; packing diagram along the pillar (bpt)-axis with potential void space shown by yellow/gray (outer/inner) colors; views of the two interpenetrated frameworks (red and green) viewed along linker (tdc^{2-})-axis and pillar (bpt)-axis, respectively.

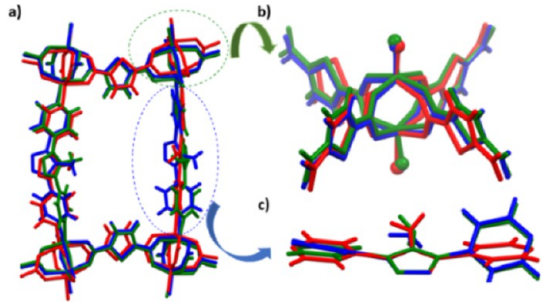

Figure 9. (a) Overlay of single frameworks emphasizing the relative distortion at metal-carboxylate junction and bpt ligand conformations on **2** (dmf) and **2**-$CHCl_3$ (**2** in red and **2**-$CHCl_3$ in green and blue). The overlays are set considering the Zn^{II} atoms on the coordination sphere (a,b), and triazole ring atoms on the bpt ligands (c) as matching atoms.

facilitates the host framework to accept chloroform solvent. Concurrently with the observed rhombohedral distortion along the pillar (bpt) axis, distinct rectangular-shaped channels (rect) emerge. As a result of the structural changes described above, the free void volume (on guest-freed structure) in the lattice decreased from 2544 $Å^3$ (35.3%) of **2** to 2264 $Å^3$ (31.6%) on **2**-$CHCl_3$ (Figure 8).

More intriguingly, in framework **2**, the dihedral angles of metal-carboxylate junctions vary from 5.2(4)−13.3(5) to 6.4(5)−12.1(5)° for O−Zn−Zn−O and to carboxylate plane (O_2−C−), respectively. However, in **2**-$CHCl_3$, the corresponding junctions are somewhat less bend with dihedral angles of 3.7(5)−12.4(7), 3.3(7)−5.6(7), 4.7(3)−12.6(6), and 8.2(4)−12.3(6)°. Concurrently, the dihedral angles between two adjacent thiophene rings (herein, designated as δ) increase from 69.5(17) to 78.5(2)° on **2** and **2**-$CHCl_3$, with increasing elongation in the rhombic grids. Another intriguing feature discerned in **2**-$CHCl_3$ is the slight subnetwork displacements. This further reflects the framework's flexibility, which is typically suggested to be driven by the combined effects of the sliding of interpenetrated nets, ligands motion, and metal-node coordination sphere changes.[1,13,39−41]

Encouraged by the successful structural evaluation of the chloroform exchange test, MOF-**2**-Zn was subjected to three new classes of organic solvents, each with different sizes and polarities as determined by the normalized (E_N^T)[42,43] value (Table S2). The resulting solvated structures were analyzed, and some generalized correlations were identified, as shown in Figure 10 and Tables S3−S6. The selected solvents comprised polar protic solvents (methanol, ethanol, isopropyl alcohol), polar aprotic solvents (acetonitrile, acetone, tetrahydrofuran, 1,4-dioxane), and one nonpolar solvent (cyclohexane).

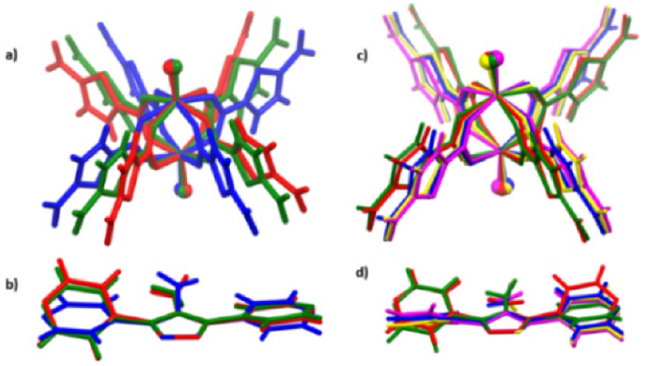

Figure 10. Overlay with emphasis on the relative distortion at metal-carboxylate junction and pillar conformations. Polar protic solvents: (a,b) **2**-MeOH (blue), **2**-EtOH (red), **2**-*i*-PrOH (green); polar aprotic and nonpolar solvents: (c,d) **2**-MeCN (red), **2**-acetone (blue), **2**-THF (green), **2**-dioxane (magenta), and **2**-cyclohexane (yellow). The overlays are set considering the Zn^{II} atoms on the coordination sphere (a,c) and triazole ring atoms on the bpt ligands (b,d) as matching atoms.

https://doi.org/10.1021/acs.cgd.3c01172
Cryst. Growth Des. XXXX, XXX, XXX−XXX

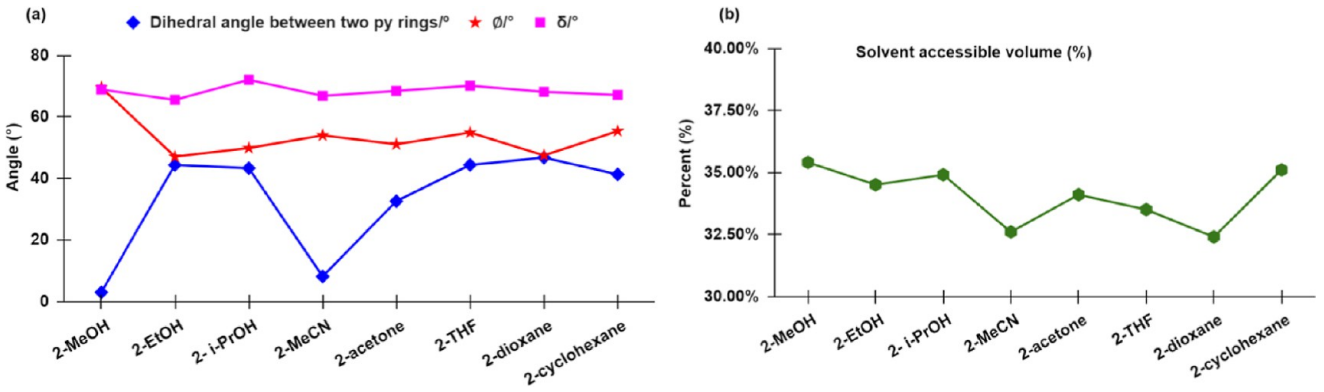

Figure 11. Comparative analysis of the structural differences between the SCSC guest exchange complexes. (a) Dihedral angles between the pyridyl rings (blue), Ø-(red), and δ-angles (pink), and (b) solvent-accessible volume (green).

Interestingly, the crystal structures revealed complete replacement of dmf molecules when using polar and polar aprotic solvents, while only partial exchange occurred with nonpolar cyclohexane. This shows the clearest evidence that the host−guest interactions depend on the proper interplay between the H-bonding donors and acceptors. Hence, with rather noninteractive cyclohexane, no proper H-bond acceptor is available for the strongly H-bonding amino group during the exchange. Therefore, a single dmf molecule per AU remains H-bonded to the $-NH_2$ group on the bpt ligand, while the remaining void is changed to cyclohexane.

In general, it can also be noted that the $-NH_2$ group and two nitrogen atoms of the triazole rings of the pillar (bpt) are disordered over two positions with approximate occupancies of 0.67:0.33 and 0.6:0.4 for **2**-MeOH and **2**-dioxane structures, respectively. Moreover, in the case of **2**-*i*-PrOH, **2**-acetone, **2**-THF, and **2**-dioxane structures, one of the pyridyl rings is disordered over two positions with its four carbon atoms having occupancy shares of 0.75:0.25, 0.6:0.4, 0.5:0.5, and 0.5:0.5, respectively. In **2**-MeCN, the tdc^{2-} linker is disordered over two positions, with its two carbon atoms sharing 0.5:0.5 occupancies.

To avoid complexity in the discussion, the following conformation analysis of the pillars considers only the structural interpretation via the dominant parts of the pillaring ligands. For further interest, all the structural values corresponding to the ligand orientations with lesser occupancies are gathered in Tables S3−S5. Unlike **2**-$CHCl_3$, all the other solvent-exchanged structures exhibit the same monoclinic space group *I*2/*a* (equal to **2**) with just marginal variations in their unit cell settings. Typically, per structure-related differences are seen as mild contractions along *β*-angle, *c*-, and *a*- or *b*-axes with simultaneous increase along *a*- or *b*-axes. Among the organic solvents employed in this study, MeCN exchanged structure **2**-MeCN is the only one manifesting contraction of all three-unit cell axes with *β*-angle reduction of −3.66%, as a result of which volumetric reduction of about −2.14% is observed for the structure. The observed shrinkage of the framework may be related to the less steric shape of the MeCN, which enables better molecular packing arrangement of the solvent molecules and adaption of the framework dimensions.

Examination of the conformation modes of the bpt ligands per different solvent exchange structures reveals that the dihedral angles between the pyridyl rings depend on the kinetic diameter of solvent molecules. For instance, smaller MeCN and MeOH molecules in **2**-MeCN and **2**-MeOH cause the pyridyl rings of the bpt ligand to adopt a near-planar orientation (dihedral angles varying ∼2−8°) in relation to each other (Figure 11). However, under the influence of steric hindrance of larger solvents, a considerable degree of variation in the tilting of the pyridyl rings is observed, as recognized in the dihedral angles ranging from ∼32 to 46°. As anticipated, these results suggest that the orientation of the pyridyl rings in the pillars is highly influenced by the molecular size of the guest solvents.[19]

Further inspection of the pillars suggests that the conformation of the amino-triazole ring is driven by its feasibility of forming host−guest interactions via H-bonding. For instance, as seen in Figure 11, while the highly polar (E_N^T = 0.762) protic and small MeOH molecules accommodate the voids, the afforded structure demonstrates a striking difference in amino-triazole ring orientation (69.6°) as compared to other solvated structures that typically covers an angular Ø range of ∼47−55°. MeOH fits perfectly in the channels with prominent host−guest interactions, enabling the $-NH_2$ group and one of the triazole nitrogen atoms to H-bond with MeOH, which also participates in intermolecular H-bonding between MeOH molecules and with the carboxyl group of the tdc^{2-} linker located in the adjacent framework (Figure S3).

As described above, the frameworks accommodating guest molecules to their confided space undergo structural alterations, which can be seen as changes in the *δ*-angles and geometric changes on the metal-carboxylate junctions (Figure 10). However, the *δ*-angles do not seem to illustrate a clear correlation with the kinetic diameter or polarity of the confined guest (Figure 11). The 2D line chart showing the comparison of the dihedral angles between the metal-carboxylate and thiophene planes in the solvated structures is presented in (Figure S4).

Figure 11b illustrates the range of solvent-accessible volumes accomplished upon different guest solvent exchanges in the host frameworks. MeOH and cyclohexane lead to larger solvent-accessible volumes, whereas MeCN exhibits the smallest void volume. The discrepancies witnessed in the voids involving two solvents (MeOH and MeCN) with near identical sizes but different E_N^T can be partially explained by the effective interactions that the highly polar MeOH molecules have with the host framework (as described above). Consequently, more H-bonds are formed with the framework, resulting in a higher number of guest molecules being accommodated inside the channels of **2**-MeOH. In the case

https://doi.org/10.1021/acs.cgd.3c01172
Cryst. Growth Des. XXXX, XXX, XXX−XXX

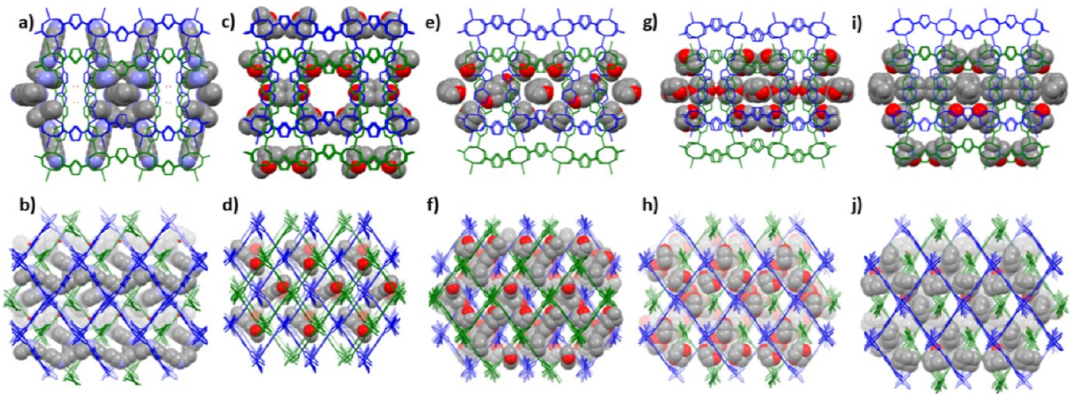

Figure 12. Illustration of solvent molecules (a,b) MeCN, (c,d) acetone, (e,f) THF, (g,h) 1,4 dioxane, and (i,j) cyclohexane/dmf mixture (in space-fill representations) filling the voids along the *a*- and *c*-axes, respectively.

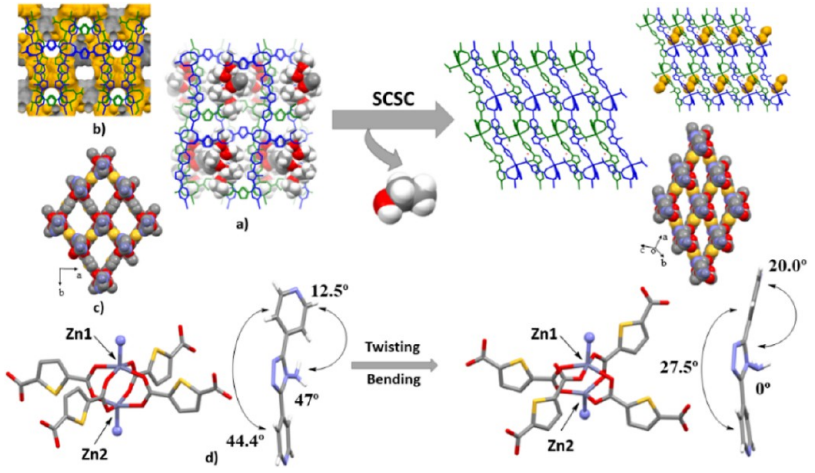

Figure 13. In response to guest removal, SCSC structural transformations between **2**-EtOH and guest-freed **2**-gf (a) along the *a*-axis, (b) potential void space visualized by yellow/gray (outer/inner) colors with two interpenetrated frameworks in blue and green, (c) a view demonstrating structural transformation when viewed along the pillar (bpt)-axis, and (d) illustration of changes in the coordination geometry of Zn^{II} nodes and bpt different angles.

of **2**-cyclohexane, wherein only partial exchange of dmf molecules resulted in a solvent mixture of dmf and cyclohexane in a 1:2 ratio, somewhat more steric crowding, and imperfect molecular packing occurs between solvent molecules that are mismatching in their size, shape, and interaction properties. Collectively, favorable framework−solvent interactions (N−H···O) and the steric hindrance imparted by solvent molecules are likely the underlying reason for the relatively larger void observed in **2**-cyclohexane. Overall, it is apparent that the pore structure is adaptive in the sense that it can accommodate various solvent guests without losing the structural integrity and crystallinity of the resulting frameworks (Figures 12 and S5).

3.3. Single-Crystal-to-Single-Crystal Guest Removal.

The observed structural changes with retained crystallinity on the solvent exchange process prompted us to explore whether crystal structure could be obtained for a solvent-free framework. Structure determination was attempted with a desolvated framework of **2**-EtOH, in which single crystals were kept at 110 °C in vacuo for 5 h. Upon visual inspection, the quality of the individual crystals was lowered significantly due to the desolvation process. Nevertheless, with few attempts, a crystal with bearable quality resulted in a data set sufficient for structure determination (see the Supporting Information).

The guest-freed crystal structure **2**-gf was solved in triclinic space group $P\bar{1}$ symmetry with two Zn^{II}, one bpt ligand, two tdc^{2-} ligands, and one water molecule in an AU. With a different symmetry, some ∼80% reduction in the unit-cell volume was observed compared to **2** (or **2**-EtOH). While the crystal structure of **2**-gf preserves the overall framework connectivity like in **2**, the network undergoes severe changes during the desolvation, contracting solvent-accessible voids to only 56 $Å^3$ (4.0%) with the transformation of the channels into discrete voids as shown in Figure 13. Accordingly, the diagonal dimensions of the channel changed from 12.71 × 16.17 Å (**2**-EtOH) to 10.50 × 16.67 Å, and the angles changed from 76.44 × 103.69° (**2**-EtOH) to 64.37 × 115.63°, joined with a considerable reduction of *δ*-angle from 65.6° (**2**-EtOH) to 36.7°, resulting in narrowing of the lozenge-shaped channels.

As evident in Figure 13, the coordination geometry of the zinc center changes dramatically. In contrast to the paddlewheel structure in **2**, the **2**-gf experiences a structural transition to the distorted paddle wheel. One Zn^{II} geometry remains in square pyramidal as in parent framework **2**, whereas the other zinc ion transforms toward distorted tetrahedral geometry with one of the bridging carboxylate groups being splintered to monodentate binding mode. Following this deformation, the ligated oxygen atoms try to enlarge their

https://doi.org/10.1021/acs.cgd.3c01172
Cryst. Growth Des. XXXX, XXX, XXX−XXX

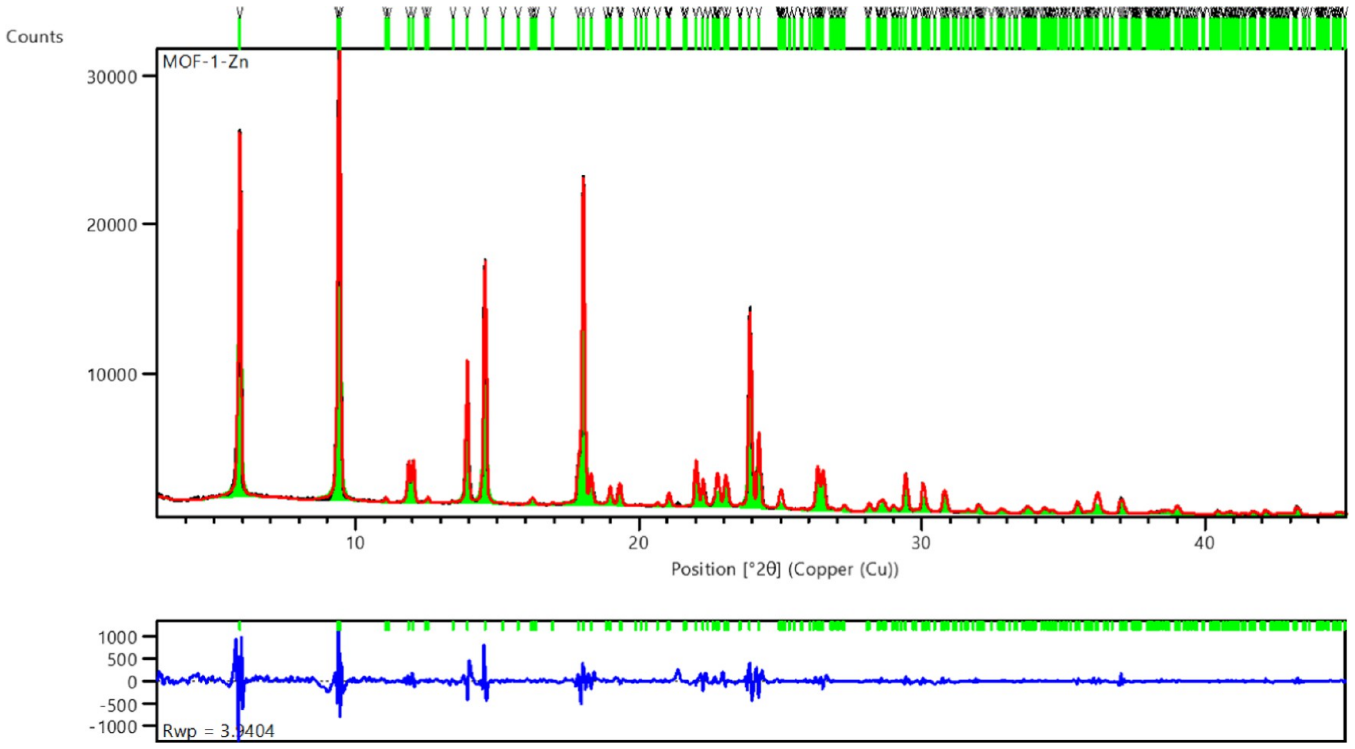

Figure 14. Pawley refinement plot of MOF-**1**-Zn. The experimental pattern is shown in black and the refined profile in red, whereas green colored markers on top correspond to characteristic Bragg peak positions of the refined unit cell of MOF-**1**-Zn. The difference plot of the experimental vs refined profile is shown below in blue.

mutual distances, having a significant distortion of adjacent ∠(O−Zn−O) bond angles. The distances for the cleaved bonds are 3.446(12) Å for *d*(Zn1−O25) and 6.014(12) for *d*(Zn2−O25), respectively. Concurrently, the two zinc atoms spacing inside the cluster changes with *d*(Zn−Zn) being 3.374(3) Å, which is markedly different from the "classical" paddlewheel unit (average 2.7 Å).[44] Somewhat similar behavior has been reported for the "classical" Zn-paddlewheel unit in case of the $Zn_2(bdc)_2L$ MOF (where L = 2,3-difluoro-1,4-bis(4-pyridyl)-benzene). The transition of the geometry from a square pyramidal to a tetrahedral geometry is accompanied by the change in *d*(Zn−Zn) from 3.00 Å (parent framework) to 3.43 Å (evacuated framework) during the "gate opening."[44,45]

In terms of structural properties, the plausible explanation for this alteration could be to compensate for the free space induced by the solvent removal, which then propagates to the bending of the strong metal−ligand bonds instead of bond cleavage.[46] By this, the **2**-gf undergoes extreme deformation, sequentially weakening and breaking one of the bonds in a bidentate carboxylic group. This deformation also leads to pillar tilting while preserving the periodic connectivity and movement of the two interpenetrated nets (Figure S6). Hence, these observations are indicative that the pillared-layer framework does not "collapse" during desolvation. Indeed, it adapts its structural conformations to minimize empty void space while maintaining its integrity as a 3D framework.

3.4. Powder X-ray Diffraction Methods. The Pawley refinements were facilitated using the Xpert HighScore Plus program to examine the purity of the studied MOFs and to confirm the correspondence of the bulk powder structures by fitting the expected unit-cell dimensions obtained by the single-crystal structures to the measured PXRD patterns. The resulting crystallographic data are tabulated in Tables S7 and S8. As verified by SCXRD data, the PXRD patterns obtained for the prepared MOFs also confirm that all three MOFs possess different structures, which can be established by the obvious differences in the respective PXRD plots (Figure S7). The high phase purity of MOF-**1**-Zn was confirmed by the excellent fit with corresponding single crystal unit cell parameters (Figure 14). For MOF-**2**-Zn, the best Pawley fit was achieved using unit cell parameters of both MOF-**1**-Zn and MOF-**2**-Zn (approximately in equal weight fraction), as shown in Figure S8. Several attempts were made to isolate MOF-**2**-Zn as a pure phase. However, none of the synthesis strategies was fully successful, as MOF-**1**-Zn and MOF-**2**-Zn either coexisted (from dominant to minor) or MOF-**1**-Zn was the sole phase evident in the PXRD patterns (Figures S26 and S27). The PXRD pattern obtained for the MOF-**3**-Zn agreed well with the corresponding SCXRD data, indicating the high phase purity of the synthesis product (Figure S9).

For most solvent-exchanged samples analyzed, the Pawley fits suggested that bulk powder is structurally consistent with corresponding SCXRD data (Figures S10−S21). For example, after immersing the mixture in chloroform, only MOF-**2**-Zn was exchanged with chloroform, supported by the PXRD pattern corresponding to **2**-$CHCl_3$ and dmf containing MOF-**1**-Zn phases. Indeed, this was also reflected by our several failed attempts to exchange a range of solvents in an SCSC manner to MOF-**1**-Zn. For MOF-**1**-Zn, the polarity, particularly the solvent size, plays an essential role in dictating the success or failure of the solvent exchange in the case of pure MOF-**1**-Zn phase. As shown by the crystal structure, dmf molecules are somewhat locked in the pore structure and are hydrogen bonded to the NH_2 group, which may limit their removal, as discussed above. After several attempts, we could

https://doi.org/10.1021/acs.cgd.3c01172
Cryst. Growth Des. XXXX, XXX, XXX−XXX

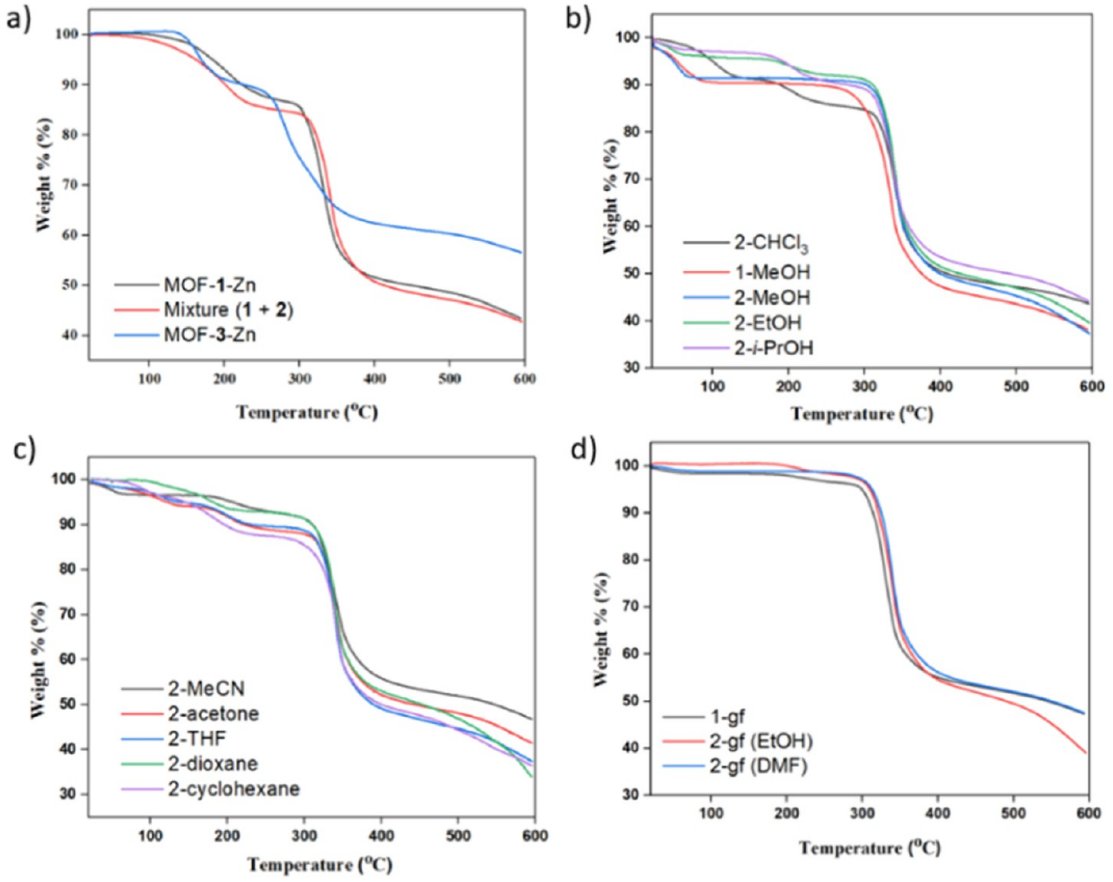

Figure 15. (a) TG curves of the MOF-**1**-Zn (black), phase mixture (MOF-**1**-Zn + MOF-**2**-Zn, red), and MOF-**3**-Zn (blue), (b) TG curves of the MOF-**1**-Zn exposed to MeOH, and phase mixture exposed to chloroform and alcohols, **2**-$CHCl_3$ (black), **1**-MeOH (red); and in case of polar protic solvents: **2**-MeOH (blue), **2**-EtOH (green), **2**-*i*-PrOH (purple), (c) TG curves of the phase mixture exposed to polar aprotic and nonpolar solvents: **2**-MeCN (black), **2**-acetone (red), **2**-THF (blue), **2**-dioxane (green), and **2**-cyclohexane (purple), and (d) TG curves of the partially desolvated MOF-**1**-Zn and phase mixture, guest-freed **1**-gf (black), guest-freed **2**-gf (EtOH, red), and guest-freed **2**-gf (dmf, blue).

successfully determine the single crystal structure for partially exchanged dmf with MeOH molecules. The obtained **1**-MeOH structure shows a rather disordered mixture of dmf and MeOH, which was also confirmed by the thermogravimetric analysis. The Pawley refinement plot for **1**-MeOH is shown in Figure S21. It can also be noted that the Pawley refinement of the PXRD pattern corresponding to **2**-MeOH bulk powder is in excellent agreement with SCXRD data of both **2**-MeOH and **1**-MeOH structures. This further proves that MOF-**1**-Zn undergoes at least partial solvent exchange when exposed to MeOH, as shown in Figure S11.

Pawley analyses of both **2**-EtOH and **2**-*i*-PrOH were consistent with unit-cell dimensions determined for corresponding SCXRD structures. Likewise, similar results were observed for all the polar aprotic and nonpolar solvents (Figures S14−S18), except for **2**-MeCN, which showed a couple of unindexed diffraction peaks in the fit, suggesting the presence of some minor unknown phase (Figure S14).

In the case of various guest-freed samples analyzed by PXRD, it is clearly seen that the **2**-EtOH sample heated at 110 °C for 5 h under vacuo (or phase mixture heated at 180 °C overnight under vacuo) shows no signs of degradation, implying that MOFs remains intact even after being subjected to high-temperature heating for extended hours. However, after the desolvation process, both examples still contained some dmf, indicating that it is challenging to remove from the pore structure of MOF-**1**-Zn. For the solvated and solvent-evacuated PXRD patterns, the refined unit-cell parameters of PXRD and SCXRD data are tabulated in Tables S7 and S8, suggesting that subtle changes in unit-cell dimensions originate from the framework flexibility.

3.5. Thermogravimetry. The thermal stability of studied materials was evaluated using thermogravimetric analyses at 10 °C min^{-1} under a N_2 flow. All pillared-layer MOFs and the products from solvent exchange tests were analyzed using this method. Representative TG runs for MOF-**1**-Zn, phase mixture, and MOF-**3**-Zn are demonstrated in Figure 15. The determined onset decomposition temperatures for the studied MOFs appear <310 °C and can be arranged in the following series: MOF-**3**-Zn (257.25 °C) < MOF-**1**-Zn (298.38 °C) < phase mixture (309.84 °C). MOF-**1**-Zn starts to lose weight between ∼84 and 282 °C, demonstrating a weight loss of 13.54 wt % (calcd. 13.36%) assigned to releasing dmf trapped in the pores. However, the phase mixture sample and MOF-**3**-Zn loss dmf between ∼70−269 and 120−247 °C corresponding to weight losses of 14.70 wt % (calcd. 15.63%) for the phase mixture (assuming a 1:1 ratio), and 11.61 wt % (calcd. 12.93%) for MOF-**3**-Zn, respectively. Above the given temperatures, gradual weight loss can be seen, seemingly involving the breakdown of organic moieties. The loss of solvent up to the temperature of 282 °C (bp of dmf 153° vs 282 °C for its desolvation) in the case of the MOF-**1**-Zn confirms the strong interaction of dmf with the framework as mentioned above.

https://doi.org/10.1021/acs.cgd.3c01172
Cryst. Growth Des. XXXX, XXX, XXX−XXX

Table 1. CO_2 Adsorption Experimental Conditions and the Measured Capacities

experiment	c_{CO_2} (vol %)	T_{ads} (°C)	T_{des} (°C)	$q_{CO_2,ads}$ ($mmol_{CO_2}/g$)	$q_{CO_2,des}$ ($mmol_{CO_2}/g$)
MOF-**1**-Zn	0.04	12	100	0.01 ± 0.00	0.00 ± 0.00
MOF-**1**-Zn	0.4	12	100	0.04 ± 0.00	0.05 ± 0.00
MOF-**1**-Zn	15	12	100	0.18 ± 0.11	0.16 ± 0.01[a]
phase mixture, cycle 1	15	12	100	0.24 ± 0.14	0.13 ± 0.00[a]
phase mixture, cycle 2	15	12	100	0.33 ± 0.19	0.17 ± 0.01[a]
phase mixture, cycle 3	15	12	100	0.88 ± 0.52	0.17 ± 0.01[a]

[a]Measured with ppm-scale sensor, thus omitting possible CO_2 desorption at concentrations above 5000 ppm.

As mentioned earlier, the solvent exchange tests were made using phase mixture samples, and considering the complexity of solvates included (guest solvent, dmf, and water impurities in some cases), it is not straightforward to calculate the correct ratios of solvents trapped inside the frameworks. However, for the comparison, the detailed wt. losses (%) observed in the respective temperature range are shown in Table S10 for all the samples. Typically, solvent-exchanged phase mixture samples demonstrate weight loss covering the region ~22−150 °C, varying by the type of the solvent and by the host−guest-related physicochemical properties prevailing in the solvated structures (more details in the Supporting Information). For instance, in **2**-$CHCl_3$, the loss of solvents proceeds in two steps, the first being from room temperature to ~142 °C (bp of $CHCl_3$ = 61.2 °C), representing the release of $CHCl_3$ from MOF-**2**-Zn phase. The second step extends to ~274 °C, indicating the gradual release of dmf from the MOF-**1**-Zn phase. Thermal decomposition of the phase mixture starts above ~307 °C (Figure 15).

Thermogravimetric analyses were also made for the solvent-freed samples (Figure 15). For the vacuo evacuated **1**-MeOH (**1**-gf), the curve is practically unchanged until ~187−268 °C, wherein modest weight loss indicates the removal of residual amounts of dmf molecules followed by initiation of thermal decomposition above 296 °C. The **2**-gf sample afforded from the evacuation of **2**-EtOH (5 h at 110 °C) shows 2.37% mass loss at 187−275 °C corresponding to the removal of dmf from the channels, indicating incomplete exchange of dmf to EtOH, as verified by the PXRD results. However, the second **2**-gf (overnight under vacuo at 180 °C) sample remained stable until 230 °C, beyond which decomposition gradually started. Based on the PXRD analyses, the sample still contains residual amounts of pristine MOF-**1**-Zn with dmf, which gradually releases the remaining dmf prior to the decomposition at ~301 °C (Table S10).

3.6. CO_2 Adsorption Studies. Based on the literature, incorporating thiophene moieties in the MOFs has enhanced CO_2 and improved CO_2/N_2 adsorption selectivity owing to the induced dipole interactions.[23,47] Hence, we hypothesize that the available pendant NH_2 group of the bpt ligand might be capable of interacting with quadrupolar CO_2. In addition, channels decorated with polarizable sulfur atoms realized in these MOFs may bind CO_2 via an induced dipole interaction. Therefore, considering these framework−CO_2 interactions that may prove beneficial in CO_2 sorption experiments, we carried out the CO_2 adsorption tests using a custom-built fixed-bed adsorption/desorption device under dry 400, 4000 ppm, and 15% CO_2 balanced with N_2 (more details in the Methods).

However, the experimental CO_2 adsorption capacities measured for both samples were relatively low, as shown in Table 1. In the ultradilute region, CO_2 adsorption on MOF-**1**-Zn is nearly negligible, resulting in only around 0.04−0.05 $mmol_{CO_2}/g_{MOF}$ at 4000 ppm, while at 400 ppm, the measured capacities were close to zero. At 15% CO_2, around 0.2 $mmol_{CO_2}/g_{MOF}$ is measured in adsorption and desorption phases for the pure MOF-**1**-Zn. Based on the above observations, only 15% CO_2 condition was tested for the phase mixture samples. With three repeats made for the phase mixture samples, CO_2 adsorptions ranged from around 0.2 up to 0.9 $mmol_{CO_2}/g_{MOF}$, imparting that the %-scale measurement had a high uncertainty. However, the desorption results for the MOF-**1**-Zn and the phase mixture are comparable, although the possibility of unaccounted CO_2 desorption should be considered, as mentioned in the Methods section. Indeed, the main reason for the high uncertainty in the %-scale measurements was the small amount of sample combined with the low adsorption capacity of the samples, which is why the response curves with and without sample differed only slightly, as shown in Figure 16.

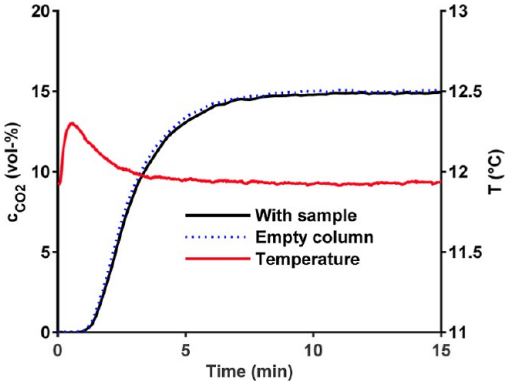

Figure 16. Adsorption breakthrough data using 15% CO_2 on MOF-**1**-Zn.

These results suggest that the samples do not host a significant CO_2 adsorption performance in postcombustion capture (PCC) conditions, let alone in direct air capture conditions. Presumably, this might be associated with a shrunk framework after solvent evacuation, resulting in severe channel contraction that could hamper CO_2 diffusion. It is worth noting that these tests were conducted below room temperature (12 °C), though this temperature is not relevant for the PCC scenario. Likely, the CO_2 uptakes are expected to be even lower at higher temperatures since the adsorption-based process is exothermic, and CO_2 uptake reduces at elevated temperatures. However, to properly characterize the CO_2 adsorption performance of the samples, a larger amount of measurement points at higher partial pressures should be conducted at different temperatures. This is especially true for the pressure-swing adsorption application of flexible MOFs,

https://doi.org/10.1021/acs.cgd.3c01172
Cryst. Growth Des. XXXX, XXX, XXX−XXX

which may have steep isotherm shapes at certain partial pressure ranges.[23,41]

4. CONCLUSIONS

In conclusion, three new mixed-ligand MOFs from identical components have been synthesized and structurally characterized. The resulting interpenetrated 3D MOFs exhibit different coordination environments around the Zn node, ranging from trigonal bipyramidal and square pyramidal to octahedral. Additionally, various binding modes were observed for the thiophene carboxylate ligand, including monodentate, bidentate, and bridge binding modes. Interestingly, structural variations associated with network topologies, and in turn intermolecular and intramolecular interactions, manifested significant differences between the MOFs, for instance, in forms of void spaces (varying from ∼23 to 35%) and solvent-exchange properties being robust for MOF-**2**-Zn structure type but severely restricted in MOF-**1**-Zn.

We further elaborated that pillared-layer MOF-**2**-Zn, entailing elastic paddlewheel building units, which readily undergoes single-crystal-to-single-crystal transformation upon guest exchange of dmf solvent with chloroform and eight other solvents of distinct kinetic diameters and different polarities, including polar protic and aprotic, as well as nonpolar solvents. Intriguing structural peculiarities in the frameworks were realized through molecular conformations of the pillar and distortion at the metal-carboxylate junction.

Interestingly, the SCXRD studies revealed that the integration of MeOH into the channels subtly directs the orientation of the NH_2-triazole core, favoring guest−guest, host−host (adjacent H-bond acceptors on the thiophene carboxylates), and host−guest interactions with the solvent guest. Additionally, the mutual effect of steric hindrance and weak interactions imposed by relatively larger solvents leads to the tilting of pyridyl rings and a less favored orientation of the triazole core. MOF-**2**-Zn showed a specific differentiation between polar and nonpolar solvents, indicating the clearest evidence of host−guest interactions. Altogether, upon different guest solvent exchanges, we observed that the void space adapts depending on the solvent type via the framework's flexibility.

Furthermore, we illustrated how, in the guest release process, a SCSC transformation takes place. In the case of solvent-emptied MOF (e.g., **2**-EtOH to **2**-gf), the structure had undergone severe contraction during the evacuation, showing significantly diminished solvent-accessible voids and transforming the channels into discrete voids. The structural changes are attributed to the variation of alterations such as deformation in paddlewheel moiety, the transformation of channel shape and sizes, and the closer proximity of two interpenetrated nets. This is a notable example showing the fragility of $\{Zn_2\}$-"paddlewheel" triggered by MOF solvent evacuation. More importantly, we demonstrate that the pillared-layer framework sustains its crystallinity and 3D networked structure under vacuum and heating-assisted desolvation.

Overall, a detailed picture of the different framework−guest interactions was accomplished via SCXRD, PXRD, and TG analyses, providing meaningful insights into a system that behaves adaptively while illustrating subtle structural transformations induced by the solvent molecules. The key properties demonstrated in this study are desirable in applications that depend on understanding how MOFs respond to external stimuli, like molecular sensing, catalysis, and separation. It is anticipated that the presented results will not only broaden the knowledge of structural isomers in MOF synthesis but also foster the understanding of delicate host−guest chemistry that plays a critical role in MOF changing its geometrical features.

■ ASSOCIATED CONTENT

Supporting Information

The Supporting Information is available free of charge at https://pubs.acs.org/doi/10.1021/acs.cgd.3c01172.

Material syntheses; crystallographic data; H-bonding scheme and topological representation of MOF-3-Zn; description of the crystal structure of 2-$CHCl_3$; physical properties of guest-exchanged solvents; H-bonding scheme in 2-MeOH; the comparison of the dihedral angle between the Zn-carboxylate and the thiophene plane between the SCSC guest exchange complexes; illustration of solvent molecules in **2**-MeOH, **2**-EtOH, and **2**-*i*-PrOH; interpenetrated frameworks of **2**-EtOH and guest-freed **2**-gf; comparative analysis of the structural differences between crystal structures; comparison of crystal data parameters between crystal structures; PXRD patterns and Pawley refinement plots; synthesis optimization and scale-up; summary of products obtained by altering metal-to-ligand ratios and concentrations; thermogravimetric results; FT-IR spectroscopy; and TopoPro output files for MOF-1-Zn, MOF-2-Zn, and MOF-3-Zn (PDF)

Accession Codes

CCDC 2279896−2279909 contain the supplementary crystallographic data for this paper. These data can be obtained free of charge via www.ccdc.cam.ac.uk/data_request/cif, or by emailing data_request@ccdc.cam.ac.uk, or by contacting The Cambridge Crystallographic Data Centre, 12 Union Road, Cambridge CB2 1EZ, UK; fax: +44 1223 336033.

CCDC 2279896−2279909 contains the supplementary crystallographic data for this paper. These data can be obtained free of charge via http://www.ccdc.cam.ac.uk/data_request/cif, or by emailing data_request@ccdc.cam.ac.uk, or by contacting The Cambridge Crystallographic Data Centre, 12 Union Road, Cambridge CB21EZ, UK; fax: + 44 1223 336033.

■ AUTHOR INFORMATION

Corresponding Author

Manu Lahtinen − *Department of Chemistry, University of Jyväskylä, FI-40014 Jyväskylän, Finland;* orcid.org/0000-0001-5561-3259; Email: manu.k.lahtinen@jyu.fi

Author

Shreya Mahajan − *Department of Chemistry, University of Jyväskylä, FI-40014 Jyväskylän, Finland*

Complete contact information is available at: https://pubs.acs.org/10.1021/acs.cgd.3c01172

Notes

The authors declare no competing financial interest.

■ ACKNOWLEDGMENTS

The authors gratefully acknowledge Jere Elfving (Research Scientist at VTT Technical Research Centre of Finland) for

conducting and analyzing the CO_2 adsorption tests and the meaningful suggestions contributing to the manuscript quality. This study was financially supported by the Academy of Finland (decision number 329314) and the University of Jyväskylä.

REFERENCES

(1) Senkovska, I.; Bon, V.; Abylgazina, L.; Mendt, M.; Berger, J.; Kieslich, G.; Petkov, P.; Luiz Fiorio, J.; Joswig, J.; Heine, T.; Schaper, L.; Bachetzky, C.; Schmid, R.; Fischer, R. A.; Pöppl, A.; Brunner, E.; Kaskel, S. Understanding MOF Flexibility: An Analysis Focused on Pillared Layer MOFs as a Model System. *Angew. Chem., Int. Ed.* **2023**, *62* (33), No. e202218076.

(2) Dong, J.; Wee, V.; Zhao, D. Stimuli-Responsive Metal-Organic Frameworks Enabled by Intrinsic Molecular Motion. *Nat. Mater.* **2022**, *21* (12), 1334−1340.

(3) Mahajan, S.; Lahtinen, M. Recent Progress in Metal-Organic Frameworks (MOFs) for CO_2 Capture at Different Pressures. *J. Environ. Chem. Eng.* **2022**, *10* (6), 108930.

(4) Bavykina, A.; Kolobov, N.; Khan, I. S.; Bau, J. A.; Ramirez, A.; Gascon, J. Metal-Organic Frameworks in Heterogeneous Catalysis: Recent Progress, New Trends, and Future Perspectives. *Chem. Rev.* **2020**, *120* (16), 8468−8535.

(5) Lawson, H. D.; Walton, S. P.; Chan, C. Metal-Organic Frameworks for Drug Delivery: A Design Perspective. *ACS Appl. Mater. Interfaces* **2021**, *13* (6), 7004−7020.

(6) Nalaparaju, A.; Jiang, J. Metal-Organic Frameworks for Liquid Phase Applications. *Adv. Sci.* **2021**, *8* (5), 2003143.

(7) Kreno, L. E.; Leong, K.; Farha, O. K.; Allendorf, M.; Van Duyne, R. P.; Hupp, J. T. Metal-Organic Framework Materials as Chemical Sensors. *Chem. Rev.* **2012**, *112* (2), 1105−1125.

(8) Li, X.; Liu, Y.; Wang, J.; Gascon, J.; Li, J.; Van der Bruggen, B. Metal-Organic Frameworks Based Membranes for Liquid Separation. *Chem. Soc. Rev.* **2017**, *46* (23), 7124−7144.

(9) Morris, R. E.; Brammer, L. Coordination Change, Lability and Hemilability in Metal-Organic Frameworks. *Chem. Soc. Rev.* **2017**, *46* (17), 5444−5462.

(10) Chen, Y.; Idrees, K. B.; Son, F. A.; Wang, X.; Chen, Z.; Xia, Q.; Li, Z.; Zhang, X.; Farha, O. K. Tuning the Structural Flexibility for Multi-Responsive Gas Sorption in Isonicotinate-Based Metal-Organic Frameworks. *ACS Appl. Mater. Interfaces* **2021**, *13* (14), 16820−16827.

(11) Zhang, J.-P.; Liao, P.-Q.; Zhou, H.-L.; Lin, R.-B.; Chen, X.-M. Single-Crystal X-Ray Diffraction Studies on Structural Transformations of Porous Coordination Polymers. *Chem. Soc. Rev.* **2014**, *43* (16), 5789−5814.

(12) Grape, E. S.; Xu, H.; Cheung, O.; Calmels, M.; Zhao, J.; Dejoie, C.; Proserpio, D. M.; Zou, X.; Inge, A. K. Breathing Metal-Organic Framework Based on Flexible Inorganic Building Units. *Cryst. Growth Des.* **2020**, *20* (1), 320−329.

(13) Wang, S.-Q.; Mukherjee, S.; Zaworotko, M. J. Spiers Memorial Lecture: Coordination Networks That Switch between Nonporous and Porous Structures: An Emerging Class of Soft Porous Crystals. *Faraday Discuss.* **2021**, *231*, 9−50.

(14) Schneemann, A.; Bon, V.; Schwedler, I.; Senkovska, I.; Kaskel, S.; Fischer, R. A. Flexible Metal-Organic Frameworks. *Chem. Soc. Rev.* **2014**, *43* (16), 6062−6096.

(15) Wang, H.; Warren, M.; Jagiello, J.; Jensen, S.; Ghose, S. K.; Tan, K.; Yu, L.; Emge, T. J.; Thonhauser, T.; Li, J. Crystallizing Atomic Xenon in a Flexible MOF to Probe and Understand Its Temperature-Dependent Breathing Behavior and Unusual Gas Adsorption Phenomenon. *J. Am. Chem. Soc.* **2020**, *142* (47), 20088−20097.

(16) Ding, B.; Wang, Y. Y.; Liu, S. X.; Wu, X. X.; Zhu, Z. Z.; Huo, J. Z.; Liu, Y. Y. A Series of Multi-Dimensional Metal-Organic Frameworks with trans-4,4′-Azo-1,2,4-Triazole: Polymorphism, Guest Induced Single-Crystal-to-Single-Crystal Transformation and Solvatochromism. *CrystEngComm* **2015**, *17* (29), 5396−5409.

(17) Ju, H.; Habata, Y.; Lee, S. S. Temperature-Dependent Supramolecular Isomeric Zn(II)-Metal-Organic Frameworks and Their Guest Exchange. *Cryst. Growth Des.* **2020**, *20* (7), 4640−4648.

(18) Manos, M. J.; Kyprianidou, E. J.; Papaefstathiou, G. S.; Tasiopoulos, A. J. Insertion of Functional Groups into a Nd^{3+} Metal-Organic Framework via Single-Crystal-to-Single-Crystal Coordinating Solvent Exchange. *Inorg. Chem.* **2012**, *51* (11), 6308−6314.

(19) Mahajan, S.; Marttinen, A.; Forsblom, S.; Lahtinen, M. Inorganic Anion-Mediated Supramolecular Entities of 4-Amino-3,5-Bis(4-Pyridyl)-1,2,4-Triazole Salts Assisted by the Interplay of Noncovalent Interactions. *Cryst. Growth Des.* **2023**, *23* (7), 5144−5162.

(20) Goswami, R.; Mandal, S. C.; Seal, N.; Pathak, B.; Neogi, S. Antibiotic-Triggered Reversible Luminescence Switching in Amine-Grafted Mixed-Linker MOF: Exceptional Turn-on and Ultrafast Nanomolar Detection of Sulfadiazine and Adenosine Monophosphate with Molecular Keypad Lock Functionality. *J. Mater. Chem. A* **2019**, *7* (33), 19471−19484.

(21) Lee, L.-W.; Kao, Y.-C.; Chung, M.-Y.; Chang, B.-C.; Lee, G.-H.; Peng, S.-M.; Wang, C.-M.; Liu, Y.-H.; Lee, S.-L.; Lu, K.-L. Rare Metal-Ion Metathesis of a Tetrahedral Zn(II) Core of a Noncentrosymmetric (3,4)-Connected 3D MOF. *Dalton Trans.* **2019**, *48* (6), 1950−1954.

(22) Qin, B.; Zhang, X.; Zhang, J. A New Multifunctional Zinc-Organic Framework with Rare Interpenetrated Tripillared Bilayers as a Luminescent Probe for Detecting Ni^{2+} and PO_4^{3-} in Water. *Cryst. Growth Des.* **2020**, *20* (8), 5120−5128.

(23) Shi, Y.-X.; Li, W.-X.; Zhang, W.-H.; Lang, J.-P. Guest-Induced Switchable Breathing Behavior in a Flexible Metal-Organic Framework with Pronounced Negative Gas Pressure. *Inorg. Chem.* **2018**, *57* (14), 8627−8633.

(24) *CrysAlisPRO*; Oxford Diffraction/Agilent Technologies UK Ltd: Yarnton, England.

(25) Sheldrick, G. M. SHELXT - Integrated Space-Group and Crystal-Structure Determination. *Acta Crystallogr., Sect. A* **2015**, *71* (1), 3−8.

(26) Dolomanov, O. V.; Bourhis, L. J.; Gildea, R. J.; Howard, J. A. K.; Puschmann, H. OLEX2: A Complete Structure Solution, Refinement and Analysis Program. *J. Appl. Crystallogr.* **2009**, *42* (2), 339−341.

(27) Sheldrick, G. M. Crystal Structure Refinement with SHELXL. *Acta Crystallogr., Sect. C: Struct. Chem.* **2015**, *71*, 3−8.

(28) Macrae, C. F.; Sovago, I.; Cottrell, S. J.; Galek, P. T. A.; McCabe, P.; Pidcock, E.; Platings, M.; Shields, G. P.; Stevens, J. S.; Towler, M.; Wood, P. A. Mercury 4.0: From Visualization to Analysis, Design and Prediction. *J. Appl. Crystallogr.* **2020**, *53* (1), 226−235.

(29) Degen, T.; Sadki, M.; Bron, E.; König, U.; Nénert, G. The HighScore Suite. *Powder Diffr.* **2014**, *29*, S13−S18.

(30) Pawley, G. S. Unit-Cell Refinement from Powder Diffraction Scans. *J. Appl. Crystallogr.* **1981**, *14* (6), 357−361.

(31) Elfving, J.; Sainio, T. Kinetic Approach to Modelling CO_2 Adsorption from Humid Air Using Amine-Functionalized Resin: Equilibrium Isotherms and Column Dynamics. *Chem. Eng. Sci.* **2021**, *246*, 116885.

(32) Elfving, J.; Kauppinen, J.; Jegoroff, M.; Ruuskanen, V.; Järvinen, L.; Sainio, T. Experimental Comparison of Regeneration Methods for CO_2 Concentration from Air Using Amine-Based Adsorbent. *Chem. Eng. J.* **2021**, *404*, 126337.

(33) Elfving, J. Direct Capture of CO_2 from Air Using Amine-Functionalized Resin-Effect of Humidity in Modelling and Evaluation of Process Concepts. Ph.D. Dissertation, Lappeenranta-Lahti University of Technology LUT, 2021. https://lutpub.lut.fi/handle/10024/163524 (accessed Aug 10, 2023).

(34) Alzahrani, K. A. H.; Deeth, R. J. Density Functional Calculations Reveal a Flexible Version of the Copper Paddlewheel Unit: Implications for Metal Organic Frameworks. *Dalton Trans.* **2016**, *45* (30), 11944−11948.

(35) Bureekaew, S.; Amirjalayer, S.; Schmid, R. Orbital Directing Effects in Copper and Zinc Based Paddle-Wheel Metal Organic

https://doi.org/10.1021/acs.cgd.3c01172
Cryst. Growth Des. XXXX, XXX, XXX−XXX

Frameworks: The Origin of Flexibility. *J. Mater. Chem.* **2012**, *22* (20), 10249−10254.
(36) Blatov, V. A.; Shevchenko, A. P.; Proserpio, D. M. Applied Topological Analysis of Crystal Structures with the Program Package ToposPro. *Cryst. Growth Des.* **2014**, *14* (7), 3576−3586.
(37) Dybtsev, D. N.; Chun, H.; Kim, K. Rigid and Flexible: A Highly Porous Metal-Organic Framework with Unusual Guest-Dependent Dynamic Behavior. *Angew. Chem., Int. Ed.* **2004**, *43* (38), 5033−5036.
(38) Henke, S.; Schneemann, A.; Wütscher, A.; Fischer, R. A. Directing the Breathing Behavior of Pillared-Layered Metal-Organic Frameworks via a Systematic Library of Functionalized Linkers Bearing Flexible Substituents. *J. Am. Chem. Soc.* **2012**, *134* (22), 9464−9474.
(39) Zhu, A.-X.; Yang, Q.-Y.; Kumar, A.; Crowley, C.; Mukherjee, S.; Chen, K.-J.; Wang, S.-Q.; O'Nolan, D.; Shivanna, M.; Zaworotko, M. J. Coordination Network That Reversibly Switches between Two Nonporous Polymorphs and a High Surface Area Porous Phase. *J. Am. Chem. Soc.* **2018**, *140* (46), 15572−15576.
(40) Song, B.-Q.; Yang, Q.-Y.; Wang, S.-Q.; Vandichel, M.; Kumar, A.; Crowley, C.; Kumar, N.; Deng, C.-H.; GasconPerez, V.; Lusi, M.; Wu, H.; Zhou, W.; Zaworotko, M. J. Reversible Switching between Nonporous and Porous Phases of a New SIFSIX Coordination Network Induced by a Flexible Linker Ligand. *J. Am. Chem. Soc.* **2020**, *142* (15), 6896−6901.
(41) Yang, Q.; Lama, P.; Sen, S.; Lusi, M.; Chen, K.; Gao, W.; Shivanna, M.; Pham, T.; Hosono, N.; Kusaka, S.; Perry, J. J.; Ma, S.; Space, B.; Barbour, L. J.; Kitagawa, S.; Zaworotko, M. J. Reversible Switching between Highly Porous and Nonporous Phases of an Interpenetrated Diamondoid Coordination Network That Exhibits Gate Opening at Methane Storage Pressures. *Angew. Chem., Int. Ed.* **2018**, *57* (20), 5684−5689.
(42) Reichardt, C. Solvatochromic Dyes as Solvent Polarity Indicators. *Chem. Rev.* **1994**, *94* (8), 2319−2358.
(43) de J Velásquez-Hernández, M.; López-Cervantes, V. B.; Martínez-Ahumada, E.; Tu, M.; Hernández-Balderas, U.; Martínez-Otero, D.; Williams, D. R.; Martis, V.; Sánchez-González, E.; Chang, J.-S.; Lee, J. S.; Balmaseda, J.; Ameloot, R.; Ibarra, I. A.; Jancik, V. CCIQS-1: A Dynamic Metal-Organic Framework with Selective Guest-Triggered Porosity Switching. *Chem. Mater.* **2022**, *34* (2), 669−677.
(44) Bon, V.; Senkovska, I.; Wallacher, D.; Többens, D. M.; Zizak, I.; Feyerherm, R.; Mueller, U.; Kaskel, S. In Situ Observation of Gating Phenomena in the Flexible Porous Coordination Polymer $Zn_2(BPnDC)_2(Bpy)$ (SNU-9) in a Combined Diffraction and Gas Adsorption Experiment. *Inorg. Chem.* **2014**, *53* (3), 1513−1520.
(45) Seo, J.; Bonneau, C.; Matsuda, R.; Takata, M.; Kitagawa, S. Soft Secondary Building Unit: Dynamic Bond Rearrangement on Multinuclear Core of Porous Coordination Polymers in Gas Media. *J. Am. Chem. Soc.* **2011**, *133* (23), 9005−9013.
(46) Aggarwal, H.; Bhatt, P. M.; Bezuidenhout, C. X.; Barbour, L. J. Direct Evidence for Single-Crystal to Single-Crystal Switching of Degree of Interpenetration in a Metal-Organic Framework. *J. Am. Chem. Soc.* **2014**, *136* (10), 3776−3779.
(47) Bolotov, V. A.; Kovalenko, K. A.; Samsonenko, D. G.; Han, X.; Zhang, X.; Smith, G. L.; MCormick, L. J.; Teat, S. J.; Yang, S.; Lennox, M. J.; Henley, A.; Besley, E.; Fedin, V. P.; Dybtsev, D. N.; Schröder, M. Enhancement of CO_2 Uptake and Selectivity in a Metal-Organic Framework by the Incorporation of Thiophene Functionality. *Inorg. Chem.* **2018**, *57* (9), 5074−5082.

https://doi.org/10.1021/acs.cgd.3c01172
Cryst. Growth Des. XXXX, XXX, XXX−XXX